# Review on synergistic damage effect of irradiation and corrosion on reactor structural alloys

Hui Liu [a,b.], Guanhong Lei[a*], Hefei Huang[a,b*]

[a] Shanghai Institute of Applied Physics, Chinese Academy of Sciences, Shanghai 201800, China

[b] School of Nuclear Science and Technology, University of Chinese Academy of Sciences, Beijing 100049, China

*Corresponding Author: Guanhong Lei (leiguanhong@sinap.ac.cn);
Hefei Huang (huanghefei@sinap.ac.cn)

**Abstract:** The synergistic damage effect of irradiation and corrosion of reactor structural materials has been a prominent research focus. This paper provides a comprehensive review of the synergistic effects on the third- and fourth-generation fission nuclear energy structural materials used in pressurized water reactors and molten salt reactors. The competitive mechanisms of multiple influencing factors, such as the irradiation dose, corrosion type, and environmental temperature, are summarized in this paper. Conceptual approaches are proposed to alleviate the synergistic damage caused by irradiation and corrosion, thereby promoting in-depth research in the future and solving this key challenge for the structural materials used in reactors.

**Key words:** Irradiation and corrosion; Synergistic effect; Austenitic stainless steels; Nickel-based alloys; Reactors.

## 1. Introduction

Nuclear energy offers several advantages, including high energy density, cleanliness, and low carbon emissions. It is considered as an effective solution to the depletion of fossil fuels and the intensification of the greenhouse effect. It has gained increasing importance in global energy supply, and currently accounts for approximately 17 % of the world's electricity production [1]. Ensuring the reliability and safety of nuclear power plant operation has been the foremost consideration worldwide. However, since the 1990s, in the most widely commercialized pressurized water reactors (PWR), stress corrosion cracking has occurred in several structural components on service during routine inspection, causing significant concern [2-4]. According to the United States Institute of Electric Power, 137 stress corrosion cracking events have been recorded in the stainless-steel components of the main

circuit of PWR nuclear power plants across different countries [5,6]. The corrosion failure of the structural materials of the primary circuit in current nuclear power plants has become an increasingly significant issue, thus posing a challenge to the development of nuclear power.

The nuclear power industry has witnessed significant growth worldwide due to advancements in nuclear power technology and increasing energy demand. In the 21st century, there have been extensive considerations and discussions regarding nuclear energy safety [7]. This has led to the emergence of the fourth-generation nuclear reactors that aim to provide cleaner energy with enhanced safety and durability, reduced radioactive waste, improved economics, and higher energy efficiency. However, the operating temperature and irradiation environment of the fourth-generation reactors differ from those of the currently operating reactors. Structural materials face the critical challenges of operating at higher temperatures, stronger neutron irradiation, and more extreme corrosive environments [8]. The success of developing advanced nuclear energy in the fourth-generation reactors hinges upon the nuclear structural materials, and their transition from experimental reactors to demonstration and commercial applications. Therefore, it is of utmost significance to investigate the behavior of materials under service conditions and comprehend the evolution of material properties in combination with the irradiation and high-temperature corrosion environment of the reactor.

In addition to possessing excellent corrosion resistance, the reactor materials should undergo irradiation testing before being deployed within the reactor. Since the 1960s, researchers have focused on addressing issues such as irradiation hardening, irradiation swelling, and high-temperature helium brittleness of structural materials [9]. As research progressed, investigations into irradiation-induced stress corrosion cracking (IASCC) of materials under the combined influence of irradiation and water environment were carried out in PWR in the early 1980s [10-18]. The irradiation performance of structural materials, particularly their behavior and properties under operational conditions, has become a key factor that affects the life of reactors.

The synergistic effect of irradiation and corrosion on materials is a crucial and universally significant scientific issue in the research field of nuclear structural materials. However, owing to the diversity and complexity of its influencing factors, it is difficult to unravel its intricacies. To date, many experimental and theoretical studies have been conducted on the service behavior of structural materials subjected to irradiation and corrosive environments [19-24] in PWRs. The rupturing of an oxide film under stress is the first step in stress corrosion cracking (SCC). Therefore, it is

important to comprehensively understand the impact of irradiation on the oxidation behavior of the materials to accurately predict IASCC. Furthermore, the effect of irradiation on the intergranular and the general corrosion of alloys in aqueous environments requires further investigation. For the fourth generation of advanced nuclear reactors, the cooling media are different, which raises a widely debated scientific concern about whether irradiation accelerates or inhibits the corrosion of structural alloys in these unique environments. Studying the evolution law and mechanism of the material microstructure by subjecting it to irradiation and corrosion environment can facilitate a better understanding of the material performance and its failure in nuclear reactor environments. It can also aid in predicting the service life of materials and propose measures to improve their properties. Given the numerous studies, it is essential to comprehensively summarize the synergistic effect of irradiation and corrosion damage on nuclear structural alloys and establish a comprehensive knowledge system for the future development and exploration of advanced core structural materials.

This paper provides an overview of the reactor environment and materials, summarizes the corresponding corrosion mechanism, and emphasizes the impact of irradiation on material corrosion, taking a PWR and a fourth-generation advanced fission nuclear power molten salt reactor as examples. This paper presents the latest insights into the irradiation corrosion behavior of structural materials within reactors. It also outlines the methods that can enhance the corrosion resistance of materials and highlights the challenges faced by the structural materials used in fourth-generation nuclear reactors. Furthermore, this paper proposes strategies for controlling the synergistic damage caused by irradiation and corrosion in materials for their future applications. These findings aim to enhance our understanding of the material failure processes in reactors and expedite the development of new materials.

## 2. PWRs

### 2.1 Structural materials of PWRs

In PWRs, austenitic stainless steel and Ni-based alloys are the primary materials used for structural components, in addition to zirconium alloy fuel cladding and pressure vessel steel [1,25–27]. Table 1 presents an overview of the main materials used in the primary circuits of PWRs. Austenitic stainless steel (e.g., 304, 304L, 316, 316L) with good corrosion resistance is utilized as an in-core structural material. Ni-based alloys, such as 600, 800, and 690, are employed for screws, pins, locating keys, and steam generator tubes in the core components due to their remarkable mechanical properties and resistance to intergranular stress corrosion cracking (IGSCC) [26]. Table

2 compares the chemical composition of the Ni-based alloys 600, 800, and 690. The Ni-based alloy 690, which has a high Cr content, exhibits superior IGSCC resistance and is therefore the preferred material for steam generator tubes in nuclear power plants. Zirconium-based alloys, such as Zircaloy-2, Zircaloy -4, ZIRLO, and M5 alloys, are specifically selected for fuel cladding in PWRs due to their low neutron capture cross-section and excellent corrosion resistance.

Table 1. Main materials used in the primary circuit of PWRs

| Materials | | Application |
|---|---|---|
| Austenitic stainless steels | 304, 304L, 316, 316L | Reactor core, piping systems of the primary loop |
| Nickel-based alloys | Inconel alloys 600,690,800 | Tubes in the steam generator |
| Zirconium-based alloy | Zircaloy-2, Zircaloy -4, ZIRLO, M5 alloys | Fuel claddings |

Table 2. Chemical composition of the Ni-based alloys 600, 800, and 690 (wt%)

| Alloys | Element | | | | | | | | | | | |
|---|---|---|---|---|---|---|---|---|---|---|---|---|
| | Ni | Cr | Fe | C | Al | Ti | Mn | Co | Cu | Si | S | P |
| 600 | 72.8 | 15.8 | 9.6 | 0.06 | / | 0.2 | 0.82 | 0.01 | 0.01 | 0.31 | < 0.001 | 0.008 |
| 800 | 30.0-35.0 | 19.0-23.0 | ≥39.5 | ≤0.1 | 0.15-0.60 | 0.15-0.60 | ≤1.5 | / | ≤0.75 | ≤1 | ≤0.015 | / |
| 690 | 59.3 | 29.2 | 9.94 | 0.018 | 0.13 | 0.27 | 0.31 | 0.01 | <0.002 | 0.27 | <0.0005 | 0.007 |

### 2.2 Environment of a PWR

PWRs are the most widely used commercial nuclear power plants, whose core is an extreme environment composed of high-temperature, high-pressure water, and strong radiation fields that affect the water chemistry, stress, and microstructure of the core materials [1,26,28]. Table 3 lists the water chemistry parameters of the primary coolant water used in a PWR. The temperature range of the water is 280–340 ºC in PWRs. Boric acid is added as an absorbent for thermal neutrons, with the acidity offset by lithium hydroxide to maintain a pH value between 6.8 and 7.4. To suppress the radiolytic oxidation of water, hydrogen overpressure by adding 25–50 cc/kg of dissolved hydrogen (DH) is introduced in the PWR. Oxygen can be introduced into the primary loop system by adding aerated water, oxygen, or $H_2O_2$ during the plant shutdown process for the PWR [29,30]. This stabilizes the oxide, thereby reducing the release of radioactive materials into the coolant.

Table 3. Water chemistry parameters of the primary coolant water used in a PWR

| Temperature (℃) | Pressure (MPa) | PH | DH (cc/kg) | DO (ppb) |
|---|---|---|---|---|
| 280-340 | 12-16 | 6.8-7.4 | 25-50 | <100 |

### 2.3 Formation of the oxide layer

Various corrosion processes of the inner components used in a PWR during service affect the operation of the reactor [26,31–33], including the following:

- Corrosion of the fuel cladding leads to the formation of adhesive oxides that affect heat transfer. Hydrogen generated by waterside corrosion that enters the zirconium alloy nuclear fuel cladding affects the ductility and fracture toughness of the cladding owing to the precipitation of brittle hydride particles.
- General corrosion of stainless steel and Ni-based alloys. Stainless steel is considered as a core component of PWRs, and its major failure mode is IASCC. The practical IASCC threshold for austenitic stainless steel is approximately 3 dpa. No significant degradation in the stress corrosion cracking (SCC) resistance is observed when this threshold is not reached. Ni-based alloys are used in the piping of steam generators in PWRs and affect the heat transfer efficiency by forming deposits. In addition, the diffusion of Ni, Co, and other cations through the oxide leads to their release into the primary water loop. The release of $^{58}Ni$ into the primary circuit that is subjected to neutron irradiation increases the overall radioactivity of the circuit in the PWR. The formation of a passivation film on the alloy surface reduces the release of corrosion products, such as Ni cations, in the PWR.
- Intergranular oxidation of stainless steel and Ni-based alloys. Intergranular stress corrosion cracking (IGSCC) or transgranular stress corrosion cracking (TGSCC) occurs in materials, causing their degradation.

#### 2.3.1 Morphology and structure of the oxide layer

The oxide layer formed in the primary water of the simulated PWR had a double-layered structure. The inner layer was a continuous and dense Cr-rich oxide, and the outer layer was either an Fe-rich oxide (in austenitic stainless steel) or a Ni-rich oxide (in a Ni-based alloy). Both layers have spinel structures [34–41]. The thickness of the oxide layer varied from 0.1 to several μm. Figure 1 shows a schematic of the oxide layer formed on the surfaces of the stainless steel and Ni-based alloys in the simulated PWR. For austenitic stainless steel, as shown in Table 4, the outer oxide layer was composed of magnetite $Fe_3O_4$ or iron-nickel spinel oxide, whereas the chemical and crystal structures of the inner oxide layer remain controversial. The inner oxide layer was composed of either a Cr-rich face-centered cubic (fcc) phase [36,38,40,42], a hexagonal $Cr_2O_3$ [43-45], or a two-phase mixture [41,46]. Several studies have observed an enrichment of Ni at the oxide/alloy interface due to the selective oxidation and preferential movement of Cr and Fe from the alloy

[34,35,38,47]. The Cr content of the alloy determined the thickness of the oxide layer [35], as shown in Fig. 2. Generally, the higher the Cr content of the alloy, the thinner was the oxide layer that was formed [35]. For Ni-based alloys, the outer oxide layer consisted of dispersed nickel ferrite ($Ni_{(1-y)}Fe_{(2+y)}O_4$) and nickel hydroxide. The metastable solid nickel hydroxide and ferric hydroxide formed on the surface could be caused by the precipitation of stable neutral aqueous complexes[48–51]. The reaction can be expressed as follows [48–51]:

$$Ni(OH)_{2(aq)} \rightleftarrows Ni(OH)_2 \quad (1)$$

$$Fe(OH)_{2(aq)} \rightleftarrows Fe(OH)_2 \quad (2)$$

$$(2+y)Fe(OH)_2 + (1-y)Ni(OH)_2 \rightleftarrows Ni_{(1-y)}Fe_{(2+y)}O_4 + 2H_2O + H_{2(aq)} \quad (3)$$

The inner oxide layer was composed of Fe-rich and contained nickel chromite ($Ni_{(1-x)}Fe_xCr_2O_4$). As can be seen from Fig. 1(b), $Cr_2O_3$ particles were unevenly distributed at the interface between the inner oxide film and the substrate. The number of $Cr_2O_3$ particles was related to the defects on the substrate surface. Some studies have also observed that there is no chromium depletion at the alloy/oxide interface [52–54]. Nevertheless, a Cr-depleted zone was observed beneath the oxide scale. A disturbed microstructure of the alloy with small grains and a strong dislocation density was observed in this Cr-depleted layer [52,54].

Table 4. Composition and structure of the oxide layer formed on the surface of austenitic stainless steel as observed from previous studies

| Material | Corrosion environment | | | | Oxide film | | | Ref |
|---|---|---|---|---|---|---|---|---|
| | T (℃) | P (MPa) | DH (cc/kg) | Time (h) | Outer layer | Inter layer | | |
| | | | | | Composition | Composition | Structure | |
| 316L | 325 | 15.5 | 18 | 1-24 | $Fe_3O_4$ | $Fe_{1.5}Cr_{1.5}O_4$ | FCC | [42] |
| 316L | 350 | 10.3 | 18 | 2000 | $Ni_{0.75}Fe_{2.25}O_4$ | $Cr_2O_3$、$FeCr_2O_4$、$Fe_3O_4$ | Hexagonal、FCC | [41] |
| 316 | 320 | 11 | 1-45 | 245-500 | $Fe_3O_4$ | $FeCr_2O_4$ | FCC | [38] |
| 304 | 260 | 10.5 | 45 | $10^3$-$10^4$ | $(Ni_{0.2}Fe_{0.8})(Fe_{0.95}Cr_{0.}$ | $(Ni_{0.2}Fe_{0.8})(Cr_{0.75}$ | FCC | [40] |

| | | | | | | | | |
|---|---|---|---|---|---|---|---|---|
| | | | | | $_{05})_2O_4$ | $Fe_{0.3})\ O_4$ | | |
| 304L | 340 | 20 | 30 | 500 | $Fe_3O_4$ | $Fe(Cr,\ Ni)_2O_4$ | FCC | [36] |
| 304 | 100-350 | / | 26 | / | Metal hydroxides, Oxyhydroxides | $Cr_2O_3$ | Hexagonal | [43] |

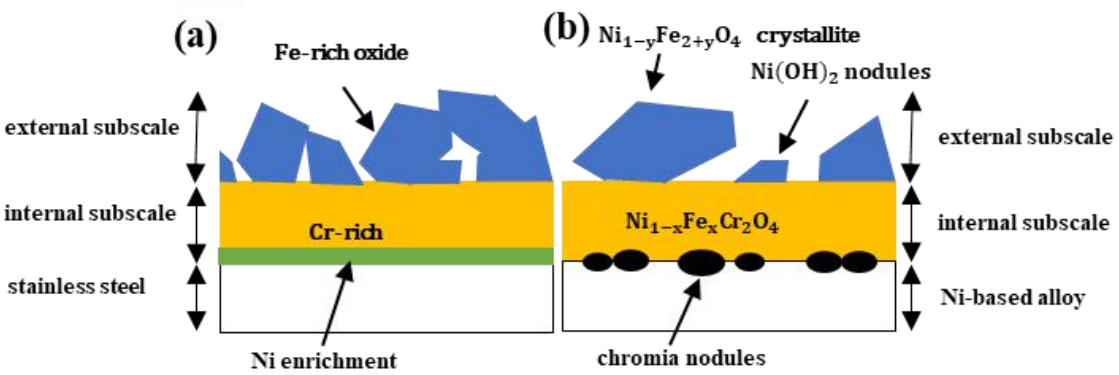


Fig. 1. Schematic of the oxide layer formed on the surface of (a) stainless steel and (b) Ni-based alloys [50] in a simulated PWR environment. *x* and *y* represent coefficients that are related to the number of Fe, Ni, and Cr atoms in the studied medium.

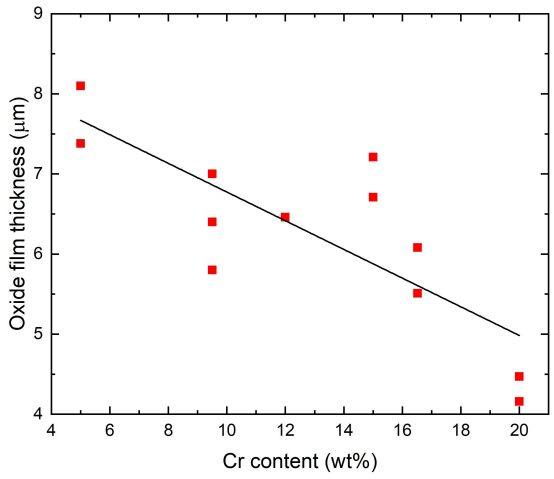


Fig. 2. Effect of Cr content on the inner oxide film thickness exposed in the simulated PWR primary water at 320 ℃ for 380 h [35].

### 2.3.2 Formation and growth of the oxide layer

The passivation process of metals in a solution is initiated with the adsorption of anions, especially $OH^-$. Previous studies [55-57] have indicated that the process of forming an oxide layer on the surface of the Fe-Cr-Ni alloys, such as stainless steel, in a simulated PWR mainly relies on the diffusion of the alloying elements Fe, Cr, and

Ni. The growth of the outer oxide layer formed on the alloy surface occurs via the dissolution and reprecipitation mechanism, whereas that of the inner oxide layer occurs via the solid growth mechanism [39,42,55]. Figure 3 schematically illustrates the oxide formation process on the stainless steel exposed to the environment inside a simulated PWR. During the initial stage of corrosion, when the material is exposed to high-temperature and high-pressure water, the oxygen in the environment comes into direct contact with the metal surface of the material. Among the alloying elements, Cr exhibits the strongest affinity for oxygen to form oxides. Consequently, during the initial stage, the material surface gradually develops a Cr-enriched oxide film. Due to the diffusion rate in oxides, Fe > Ni >> Cr [39,42,55], the comparatively faster diffusion rate of Fe results in its diffusion outward into the aqueous medium or its interaction with adsorbed $H_2O$, eventually precipitating into the outer oxide particles. At the same time, external oxygen diffuses into the interior of the matrix material and reacts with Cr to form an inner oxide film. Considering that the diffusion rate of Ni in the inner oxide film lies between that of Cr and Fe, Ni neither accumulates extensively within the inner layer nor exists in significant quantities within the outer oxide layer. Consequently, the outer oxide layer is predominantly composed of Fe, whereas the inner oxide film is enriched with Cr. Thin Ni enrichment may occur at the metal oxide/interface, depending on the diffusion rate of Ni.

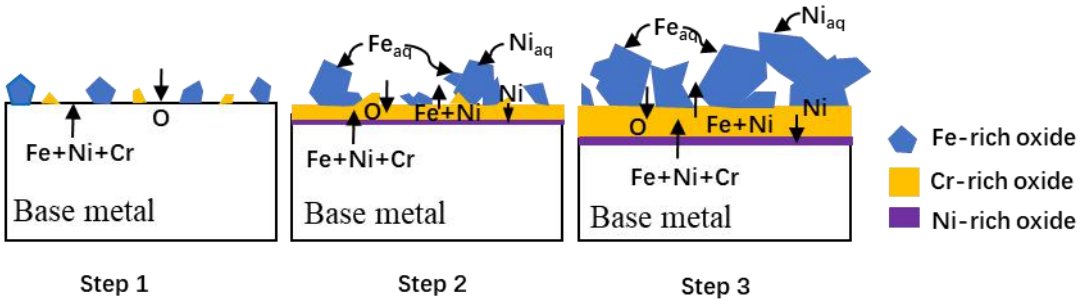


Fig. 3. Schematics showing the formation process of the oxide on stainless steel exposed to a simulated PWR environment.

The factors affecting the growth of the oxide layers in the simulated PWR are summarized in Table 5. The chemical parameters of water (DH [29,58-63], DO [29, 64-66], and PH[56, 67,68]) are the key factors affecting the corrosion resistance and properties of the oxide in a PWR primary system. Among these parameters, the DH is a favorable factor for reducing the oxidation rate. In particular, the primary water undergoes radiolysis when it is subjected to irradiation, producing oxidizing species ($O_2$ + $H_2O_2$) and making the corrosion electric displacement more positive, which, in turn, increases the corrosion rate. Irradiation affects the corrosion behavior of materials by

changing the water environment, as will be discussed in detail in Section 2.4.3.

Matthews et al. [69] suggested that the reaction rate at the interface is the principal factor affecting the oxide growth, surpassing other contributing factors. The oxide growth depends on the interfacial reaction rate when the same sample is simultaneously exposed to the PWR environment for the same time. According to the point-defect model proposed by Macdonald et al. [70], in high-temperature and high-pressure water environments, oxygen ion vacancies can be formed at the interface between the inner oxide layer and the base metal through reaction (4) [51,70]. The metal atoms are converted into metal-ions via reactions (4)–(6) [51,70,71].

$$\mathrm{m} \leftrightarrow m^{x}_{m\ (oxide)} + V^{\cdot\cdot}_{O\ (oxide)} + 2e^{-} \quad (4)$$

$$\mathrm{Ni} \leftrightarrow Ni^{\cdot\cdot} + 2e^{-} \quad (5)$$

$$\mathrm{Fe} \leftrightarrow Fe^{\cdot\cdot} + 2e^{-} \quad (6)$$

where m denotes the metal atom in the base metal, namely Cr, Ni, and Fe, $m^{x}_{m\ (oxide)}$ are normal metal-ion lattice sites in the inner oxide, $V^{\bullet\bullet}_{O\ (oxide)}$ represents the oxygen-ion vacancy in the oxide, and $Ni^{\cdot\cdot}$ and $Fe^{\cdot\cdot}$ are the interstitial metal cations in the inner oxide layer.

$O^{2-}$ diffuses to the oxide/matrix interface (oxygen-ion vacancies outward surface) and combines with metal cations to form the inner oxide layer, resulting in the inward migration of the oxide/matrix interface. The oxygen vacancy and cation diffusion rates control the growth rate of the inner oxide. Further, the metal cations formed in the inner oxide layer diffuse into the aqueous medium or interact with the absorbed $H_2O$ and eventually precipitate into oxide particles driven by the dissolution and redeposition mechanisms [40,65]. The diffusion rate of cations in the inner oxide layer plays a major role in the growth of the outer oxide layer. Irradiation controls the growth of the oxide by affecting the diffusion rate, as described in Section 2.4.

Table 5. Factors affecting the growth of the oxide

| Factors | Details |
|---|---|
| Water chemistry | A higher DO concentration facilitates the formation of a thicker and more porous inner oxide film [29, 64-66].<br>DH is a favorable factor for reducing the oxidation rate [29,58-63];<br>The protective property of the inner oxide film in safe potential |

| | |
|---|---|
| | (E)-pH zone increases with increasing pH value [56, 67,68]. |
| Temperature | The oxidation rate increases with temperature until it reaches a peak, but a rate inversion occurs at higher temperatures [69,72]. |
| Grain orientation | The variation in the inner oxide thickness depends on the substrate orientation and can exhibit an order-of-magnitude difference. Furthermore, the preferred substrate orientation for oxide growth varies with temperature. [69]. |
| Interfacial reactions [70] | (ⅰ) Generation of oxygen-ion vacancies and the subsequent consumption of metal cations at the film/metal interface;<br>(ⅱ) Metal cations and oxygen-ion vacancy migration through the inner oxide film;<br>(ⅲ) Dissolution or precipitation of cations at the film/medium interface. |
| Sample state | (ⅰ) Cold work, which has been found to increase the initial oxidation rate but is beneficial to inhibit long-term corrosion [72–74];<br>(ⅱ) Alloy composition, where higher the Cr concentration, greater is the corrosion resistance of the alloy [74]. |

### 2.4 Effect of irradiation on corrosion

The corrosion of the core structural materials is affected by irradiation in at least three distinct ways.

(i) Microstructural changes (formation of dislocation loops, cavities, helium bubbles, and precipitates) in alloys induced by irradiation are related to the irradiation dose and temperature. These microscale changes influence the oxidation kinetics by changing the diffusion rate of the oxygen vacancies and metal cations. Consequently, these defects have the potential to modify and expedite oxidation at the oxide/liquid and metal/oxide interfaces.

(ii) Irradiation-induced elemental segregation at the grain boundaries, such as the depletion of Cr, Fe, and Mo, and the enrichment of Si, Ni, and P, is believed to be responsible for the intergranular oxidation behavior of alloys.

(iii) Irradiation of water causes its decomposition into free radicals and oxidizing substances, which increases the corrosion potential of the aqueous medium. An increase in the corrosion potential causes the dissolution of the Cr-rich inner oxide layer of the alloys in the high-temperature water, thus leading to a higher corrosion rate.

The general corrosion behavior and the intergranular oxidation of irradiated materials have been extensively studied both domestically and internationally [75]. There is still no consensus on the effect of irradiation on the oxidation of alloys. Irradiation aggravates the corrosive environment through water radiolysis and accelerates the corrosion of materials by introducing microstructural damage and microchemical segregation. However, some experimental studies [76-78], have reported opposite results: irradiation inhibits the general corrosion behavior and intergranular oxidation of the material owing to differences in the experimental conditions, such as the corrosion temperature and time, ions species and doses. In addition, no significant difference has been observed in the corrosion behavior of the irradiated and unirradiated materials [21,79]. Therefore, this section reviews the role of irradiation on the general corrosion behavior and intergranular oxidation corrosion from three aspects: radiation damage, radiation-induced segregation, and changes in the water environment induced by water radiolysis.

The most effective approach for obtaining the irradiation corrosion data involves simulating the irradiated water environment. The autoclave system, capable of operating at temperatures between 280–325 $^{o}$C and high pressures ranging from 7.1 to 16.2 MPa, has proven successful in simulating the primary circuit. Ion-exchange resins are used to monitor the water chemistry in high-pressure sterilizers with recirculation loops. The level of dissolved hydrogen in the medium is assessed by measuring the thermal conductivity of water using an in situ $H_2$ sensor. The neutron irradiation experiments possess numerous difficulties and limitations to research work due to their long cycle time, high cost, and high radioactivity. In contrast, ion irradiation offers advantages such as a high damage rate, easy parameter adjustment, absence of radioactivity, and cost-effectiveness. Consequently, rapid ion implantation is commonly adopted in laboratory studies to simulate neutron irradiation and facilitate fundamental research endeavors [80], thus establishing radiation damage models and elucidating the pertinent mechanisms.

### 2.4.1 Effect of irradiation defects on corrosion

After irradiation, defects such as voids, helium bubbles, black spots, and dislocation rings are produced inside the material [75,81]. For a comprehensive understanding of the composition and structure of the oxide formed on the metal surface, as well as the depth of the inner oxide layer following irradiation, extensive studies have been conducted, which have been summarized in Table 6[19–21,76,82,83]. Although Deng et al.[20] have already reported that a finer oxide grain in the inner oxide film was formed

on a 3-dpa proton-irradiated 316 L austenitic stainless steel after exposure to the primary water of the simulated PWR for 500 h, it is generally accepted that irradiation does not alter the crystal structure and the qualitative chemistry of the inner and outer oxides formed on materials, which can be characterized using high-resolution TEM (HRTEM) [19,21,71, 77,78, 82,84,85]. Similar to the unirradiated sample, the oxide layer maintains its characteristic double-layer structure when stainless steel is irradiated. The outer layer comprises polyhedral oxide particles primarily composed of Fe-rich oxides, such as dispersed Fe-Ni spinel or magnetite $Fe_3O_4$, and the inner continuous and protective oxide film is predominantly composed of Cr-rich oxide, known as Fe-Cr-Ni spinel. Both layers have been characterized as spinel structures. In addition, Ni enrichment at the oxide/matrix interface has been observed [19,82]. However, based on the available study data [19-21,71,76,82,85,87-90], it has been observed that irradiation affects the quantitative chemistry, morphology, and thickness of the oxide layers formed on the alloys. In irradiated materials, the Cr content in the inner layer has been observed to be high [19, 76-78,85 ]. In contrast, a lower Cr content has been observed in the inner oxides of 316 L stainless steel irradiated with protons exposed to high-temperature water, due to the dissolution of Cr-rich spinel oxides in irradiated water with added hydrogen [86]. Further, no significant change in the Cr concentration in the inner oxide has been reported with increasing irradiation dose [20,21,71]. These different oxidation behaviors probably arise from the different irradiation and oxidation conditions (dose, temperature, oxidation duration, etc.) In addition to the change in the Cr concentration, Kuang et al. [78] observed that the maximum Ni content in the transition zone is higher and wider.

Table 6. Some examples of the composition and structure of the oxide formed on the metal surface after irradiation, as well as the depth of the inner oxide layer

| Alloy | Irradiation parameters | | | type | Corrosion environment | | | Oxide film | | | | Ref |
|---|---|---|---|---|---|---|---|---|---|---|---|---|
| | Ion | Dose (dpa) | Temp. (℃) | | Pressure (bar) | Time (h) | Temp. (℃) | Outer layer | Inner layer | Inner oxide layer depth (nm) | | |
| | | | | | | | | | | Unirr. | Irra. | |
| 304 | 2MeV protons | 0.5/1.5/3/5 | 360 | PWR | 155 | 500 | 320 | Fe-Ni spinel | Fe-Cr-Ni spinel | 16.7 | 39.1 (5 dpa) | [20] |
| 316L | 1.5MeV protons | 1.5 | 380 | | 155 | 24 | 325 | $Fe_3O_4$ magnetite | $(FeCrNi)_3O_4$ spinel | 42 ± 2 | 141 ± 2 | [19] |
| 316L | 240 keV Xe+ | / | / | | 155 | 200 | 325 | $Fe_3O_4$ magnetite | $FeCr_2O_4$ spinel | / | 92 | [83] |

| | | | | | | | | | | | | |
|---|---|---|---|---|---|---|---|---|---|---|---|---|
| 316L | 3MeV protons | / | / | | 155 | 1024 | 325 | $Fe_3O_4$ magnetite | Fe-Cr-Ni spinel | 90 | 60 | [77] |
| 316L | 2MeV protons | 2.5 | 360 | | 150 | | 320 | Fe-Ni spinel | Fe-Cr-Ni spinel | 193 ± 33 | 118 ± 21 nm | [79] |
| Alloy 690 | 180 keV Xe+ | / | / | | 155 | 66-858 | 325 | $NiFe_2O_4$ spinel | $(Fe,Ni)Cr_2O_4$ spinel | / | / | [84] |
| 316L | 2MeV protons | 5 | 300 | BWR | / | 70 | 288 | $(Fe,Cr)_2O_3$ | $(FeCrNi)_3O_4$ spinel | 70 ± 12 | 63 ± 16 | [21] |

Generally, these irradiation-induced defects accelerate corrosion primarily in two ways [19,20,71,83,85,87-90]: (i) by increasing the size and/or density of the outer oxide particles and (ii) by increasing the depth of the inner oxide layer. The oxidation kinetics model has been employed to elucidate the changes in the inner oxide layer thickness caused by irradiation-induced defects [71,90]. Based on the quasi-stationarity assumption [90], the thickness of the oxide scale on the surface of a nickel-based alloy in a PWR can be described using Equation (7) as follows:

$$X(t) = \sqrt{\frac{\delta \times D_{sc}^{O}}{\varphi} \times t + (X_0)^2} \quad (7)$$

where X(t) represents the thickness of the inner oxide layer, $X_0$ denotes the thickness of the initial oxide film, $t$ is the oxidation time, $\delta$ and $\varphi$ are the width and size, respectively, of the grain boundaries in the oxide. $D_{sc}^{O}$ is the diffusion coefficient of oxygen vacancies along short circuits (such as the grain boundaries in oxides). Only the grain boundaries act as channels for the diffusion of oxygen vacancies in the absence of defects. However, the grain boundaries as well as the irradiation-induced defects contribute to the diffusion of oxygen vacancies when subjected to irradiation. Therefore, it is anticipated that $D_{sc}^{O}$ will increase, indicating a higher diffusion rate of oxygen vacancies, resulting in the formation of a thicker inner oxide layer, according to Equation (7).

On the other hand, the irradiation-induced defects are the preferred nucleation points for the oxide particles, and thus the number of outer oxide particles is higher. These defects function as fast diffusion channels, facilitating the outward diffusion of metal cations. Thus, the oxide particles formed on the surface of the material are

larger than those in the unirradiated state. The oxidation kinetics provide insights into the oxidation rate. Higher oxidation kinetic values in the irradiated region indicate that irradiation accelerates the corrosion process. For example, Boisson et al. [19] reported a five-fold increase in the oxidation kinetics of irradiated 316L austenitic stainless steel compared to the unirradiated area after 24 h of oxidation in a simulated PWR. Similarly, Deng [20] emphasized that radiation enhances the oxidation kinetics (up to four times faster) during a longer oxidation duration about 500 h in irradiated 304 nuclear-grade stainless steel. Thicker inner oxide layers in the irradiated areas indicate faster oxygen diffusion. However, Perrin et al. [76] conducted an experiment where they irradiated 316L stainless steel with protons and subjected it to corrosion in a simulated PWR at 325 $^{o}$C for 1024 h. Surprisingly, they found that oxygen diffusion in the inner oxide layer of the irradiated sample occurred at a slow pace. The diffusion coefficients in the irradiated sample and unirradiated sample were $5 \times 10^{-17} \mathrm{cm}^2 \mathrm{s}^{-1}$ and $3 \times 10^{-16} \mathrm{cm}^2 \mathrm{s}^{-1}$, respectively. The outer oxide particles formed on the irradiated sample were smaller in size, and the inner oxide film was thinner than that of the unirradiated sample, as shown in Fig. 4. These observations indicate that irradiation inhibits corrosion. The growth of the inner oxide film was constrained by the slow diffusion of oxygen through the inner oxide layer. Irradiation-induced defects promoted the diffusion of Cr, resulting in the formation of a thicker Cr-rich film. A dense Cr-rich film normally acts as a protective layer that impedes oxygen diffusion and further oxidization. Kuang et al. [78] also suggested that irradiation-induced defects enhance the diffusion of Cr, resulting in higher protection of the inner oxide layer, which is one of the reasons for the enhanced oxidation resistance in the irradiated region. Further, they observed that the continuous Ni-rich zone formed near the oxide/matrix interface reduces the "available space" for oxidation. It should be noted that in the experiment conducted by Perrin et al., the samples were only mechanically polished. Samples in which cold work is induced by polishing [91,92], tend to exhibit faster oxidation kinetics. However, this cold working diminishes under irradiation [93] due to the disappearance of the initial dislocation network. Consequently, the irradiated area without cold work experiences a slower rate of oxygen diffusion, resulting in thinner oxides. Therefore, sample polishing must be strictly controlled, and the results obtained by Perrin et al. by irradiating samples with protons (or neutrons) using mechanical polishing need to be validated to determine whether polish-induced cold working overcomes the effects of irradiation.

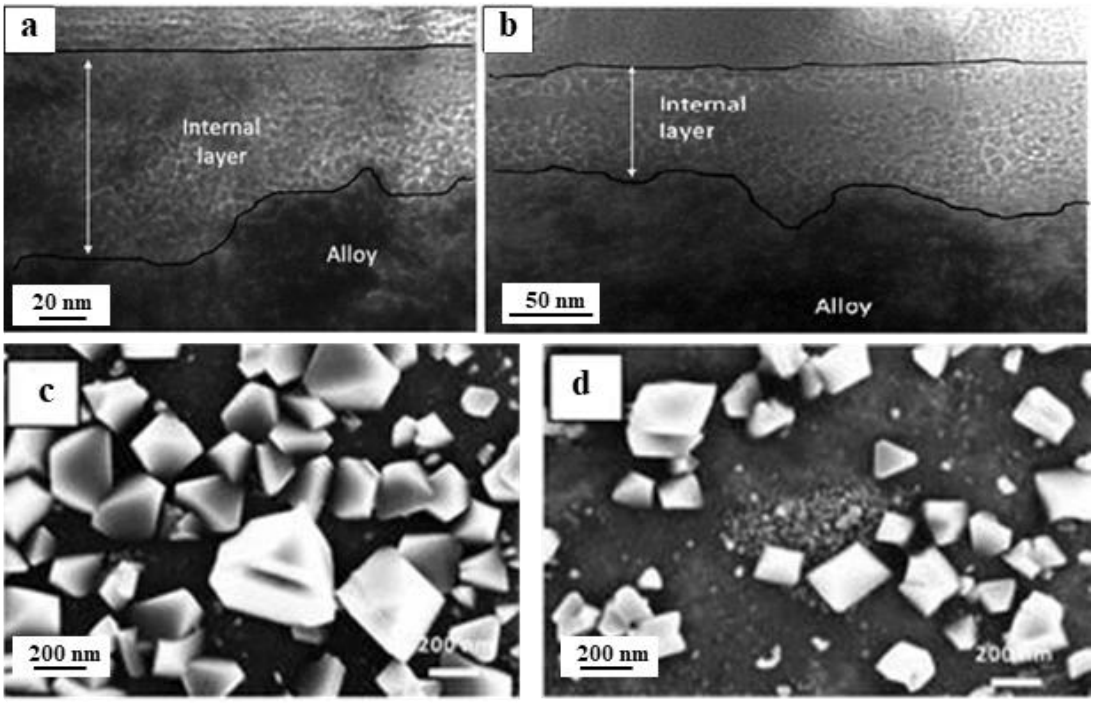


Fig. 4. Observation of the oxide in the (a), (c) unirradiated and (b), (d) irradiated 316L stainless steel corroded for 1040 h at 325 ℃ in the primary water of the simulated PWR [76].

The corrosion of the alloy intensifies with increasing corrosion time, as shown in Fig. 5(a) [82,90]. Furthermore, the density and/or size of the irradiation-induced defects are influenced by the irradiation dose or temperature. For a given material, the irradiation-induced defect density and/or size increases with increasing irradiation dose (Fig. 5(b)) or elevated irradiation temperature [20,71,87]. Consequently, the diffusion rates of the metal cations and oxygen anions increase, resulting in an elevated oxidation rate. It is worth noting that a smoother surface appears in the irradiated alloy due to irradiation-induced ion sputtering [85], as shown in Fig. 6(c). During the corrosion process, rough surfaces with large surface areas absorb more dissolved oxygen and impurities, thereby enhancing the nucleation rate of oxides. In contrast, the irradiated alloys exhibit fewer oxide particles. Simultaneously, high-energy particle irradiation causes localized temperature increases on the material surface and the formation of Cr-rich oxides (Fig. 6 (d)). The thin layer composed of Cr-rich oxide prevents the interaction between the underlying elements and external oxygen atoms, thus hindering the growth and nucleation of iron-rich oxides on the alloy surface in the initial corrosion stage (Fig. 6 (a)). In addition, the short-term diffusion of atoms becomes difficult due to defects. However, for long-term corrosion,

irradiation-induced defects promote the long-range migration of metal atoms, and thus the oxidation rate and corrosion weight gain of the irradiated alloys are higher than those of the irradiated alloys (Fig. 6(a) and 6(b)). The defects are principally point defects. Their impact on the diffusion of enhanced oxygen and metal atoms during the initial stage of corrosion is minimal, and the corrosion behavior of materials is almost unaffected by irradiation [77,79]. Jiao et al. [21] observed that proton-irradiated SUS316 stainless steel corroded for 70 h and that the thickness of the inner oxide film was only marginally affected by irradiation, as shown in Fig. 7. However, no conclusive explanation for this phenomenon was given. Further empirical research is necessary to investigate the influence of irradiation-induced defects on material corrosion, including exploration of the critical irradiation dose that either promotes, inhibits, or has no effect on material corrosion, as well as the influence and mechanism of irradiation on material corrosion at the initial stage of irradiation. This will enable obtaining a more systematic understanding of the effect of irradiation on corrosion, which has guiding significance for the application of nuclear materials in the nuclear industry.

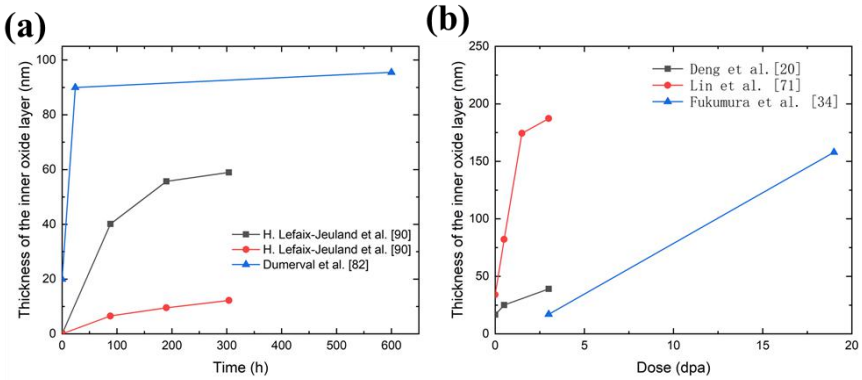


Fig. 5. Oxide thickness as a function of the (a) corrosion time [82,90] and (b) irradiation dose [20,71,87] in a simulated PWR environment.

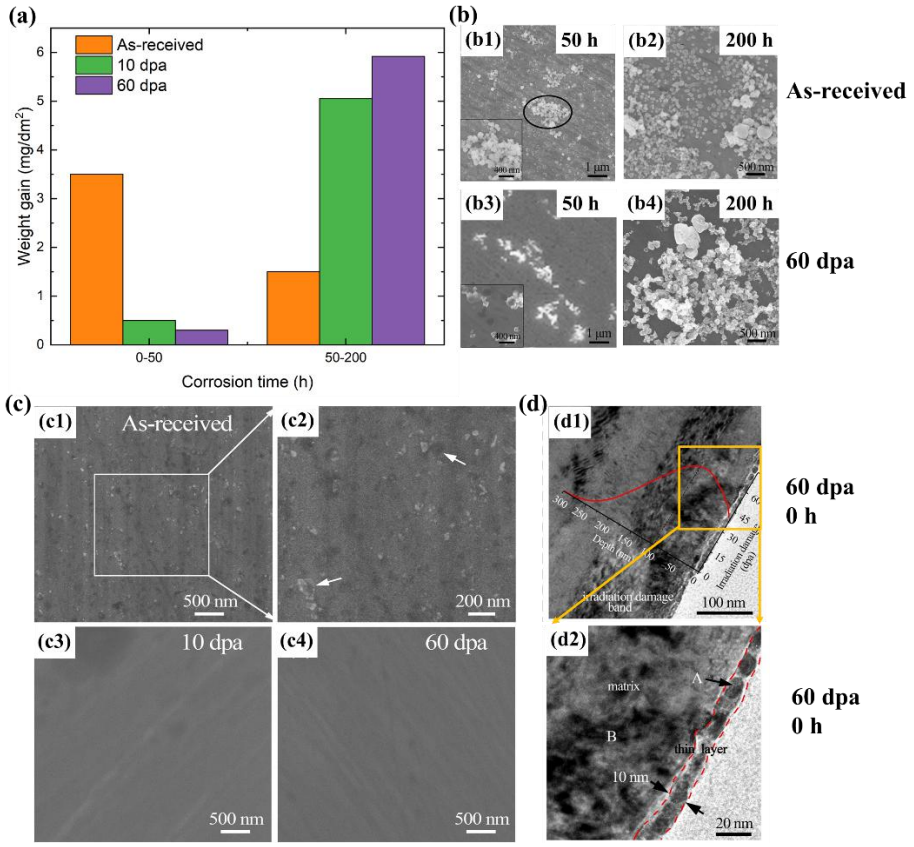


Fig. 6. (a) Histogram of weight gain of the $Fe_{16}Cr_{4.5}Al$ alloy samples with corrosion time. (b) SEM images showing the surface morphologies of the $Fe_{16}Cr_{4.5}Al$ alloy samples corroded for 50 h and 200 h (b1, b2) as-received and irradiated to (b3, b4) 60 dpa. (c) SEM images showing the surface morphologies of the $Fe_{16}Cr_{4.5}Al$ alloy samples: (c1) as-received sample and (c2) magnified images of the rectangular region in (c1), and samples irradiated to (c3) 10 dpa and (c4) 60 dpa. (d) Cross-sectional TEM bright-field images of the $Fe_{16}Cr_{4.5}Al$ alloy samples after (d1) and (d2) irradiation to 60 dpa [85].

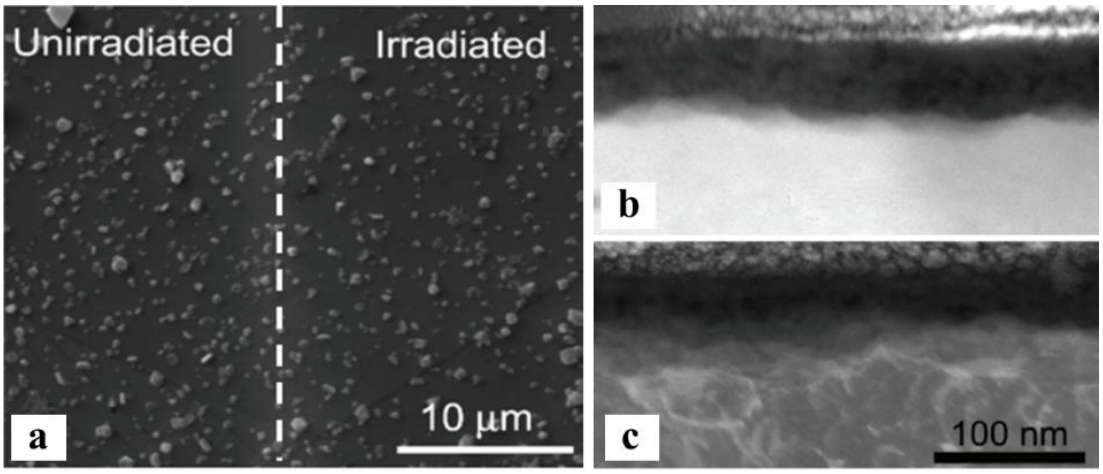


.

Fig. 7. (a) Surface morphology of the oxide scale formed on SUS316 stainless steel

with irradiated and unirradiated areas. TEM observation of the (b) unirradiated and (c) irradiated samples [21].

### 2.4.2 Effect of radiation-induced segregation on corrosion

Radiation-induced segregation (RIS) refers to the phenomenon of microchemical segregation at the grain boundaries (GB) due to irradiation, leading to the depletion of Cr, Fe, and Mo, and the enrichment of Si, Ni, and P [15,94,95]. Post-irradiation annealing eliminates element segregation at the grain boundary so that no local corrosion of the grain boundaries is observed [89]. This indicates that RIS is primarily responsible for the intergranular oxidation of materials. Grain boundaries act as the preferred pathways for diffusion and are therefore more susceptible to oxidation. Intergranular corrosion occurs in the irradiated as well as unirradiated areas, but the deeper oxide penetration in the irradiated area suggests that irradiation intensifies intergranular corrosion [19,20,87,71,96-98], which is attributed to the depletion of Cr at the grain boundaries. The lower Cr content in the grain boundary results in the increased penetration of the oxidation depth (Figs. 8 and 9) and decreases the intergranular corrosion resistance [20,87]. Furthermore, the unirradiated alloy exhibits Ni-rich regions before the oxide tip at the grain boundary, whereas such regions are not formed in the irradiated samples [20]. This observation further supports the notion that irradiation promotes a high intergranular corrosion rate. The selective oxidation of Cr and Fe leads to the preferential removal of these elements from the alloy, forming Ni-rich regions. In irradiated alloys, rapid corrosion along the grain boundaries does not provide sufficient time for selective oxidation to occur [20,99].

The depth of the intergranular oxidation increases with increasing irradiation dose (Fig. 8) [20,100], possibly because of maximum Cr consumption at the grain boundaries at higher doses. Studies [101–103] have shown that the depletion value of Cr at the grain boundary changes dramatically at low and medium doses (0.1~5 dpa) but no longer changes significantly with further increase in the radiation dose, or even remains unchanged at higher doses, as shown in Fig. 9. Fukumura et al. [87] found that the degree of Cr segregation in neutron-irradiated stainless steel exposed to a simulated PWR for 1149 h did not change significantly with the increase in dose from 25 dpa to 73 dpa, but the oxidation length at the grain boundary increased by approximately 20 %, as depicted in Fig. 8 (b). It is challenging to quantitatively explain the promotion of oxidation at the grain boundary at high irradiation doses through Cr depletion alone. The evolution of Ni and Si segregation at the grain boundaries may be implicated in the promotion of oxidation at these boundaries at

high irradiation doses (Fig. 8(b)).

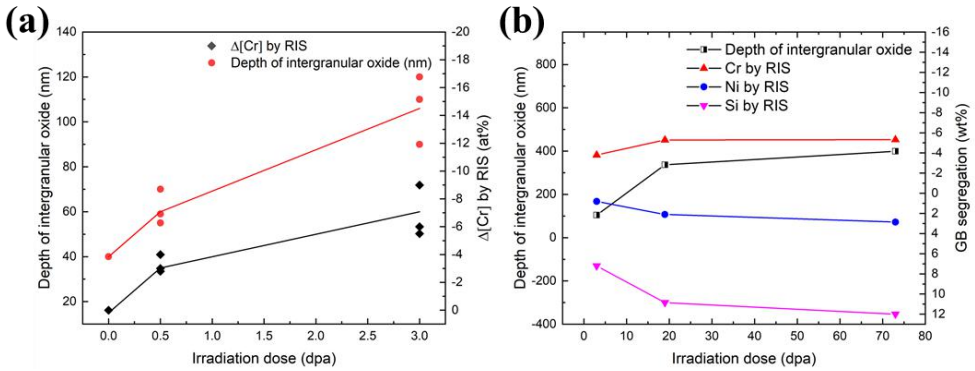


Fig. 8. Depth of the intergranular oxide and Cr segregation by RIS as a function of the irradiation dose [20,87].

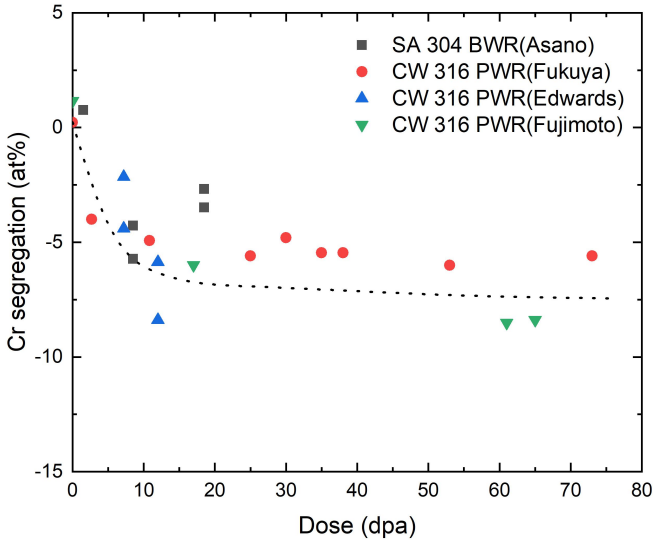


Fig. 9. Cr segregation as a function of the irradiation dose [101–103].

However, the presence of Si segregated at the irradiated grain boundary appears to inhibit intergranular corrosion. Kuang et al. [94] compared the intergranular oxidation behavior of solution annealing (SA) and 2.5 dpa proton-irradiated specimens of 316L in a simulated PWR with exposure 1000 h, and found that the penetration depth of the intergranular oxide in the irradiated area was shallower than that in the unirradiated area. This suggests that irradiation enhances the intergranular oxidation resistance of stainless steel. Figure 10 shows the intergranular oxidation process at the irradiated and unirradiated grain boundaries [94]. Researchers have proposed that Si separated at the grain boundaries of the irradiated samples tends to

diffuse outward and undergoes oxidation due to its high diffusion coefficient and affinity for oxygen. The Si-rich oxide at the intergranular oxide tip of the irradiated sample serves as a temporary diffusion barrier for oxygen, although it tends to dissolve near the sample surface. The migration efficiency of the elements (especially Cr) along the grain boundary of the irradiated sample to the oxidation front improves. This is because the preferential diffusion of Si generates vacancies, which can promote the diffusion of Cr atoms and lead to an increase in the Cr content at the tips of the intergranular oxides. Irradiation-induced structural defects also contribute to the diffusion of elements such as Cr along the grain boundary. Therefore, although Cr in the grain boundaries of the irradiated samples is depleted due to RIS at the original grain boundaries, Cr is enriched in the oxides along the grain boundaries of the irradiated samples. The coenrichment of Si and Cr at the tips of the intergranular oxides enhances oxidation resistance, ultimately leading to a decrease in the oxidation rate of the irradiated grain boundary. In addition, the grain boundary structure affects RIS [104,105] and intergranular corrosion [106]. Therefore, future experimental analyses should focus on selecting the same type of grain boundary across irradiated and unirradiated areas. This will enable direct comparative studies of the intergranular oxidation behavior between the two areas at a single grain boundary, eliminating the interference caused by the differences in the GB structure differences. This is crucial to for distinguishing the effects of irradiation on intergranular oxidation.

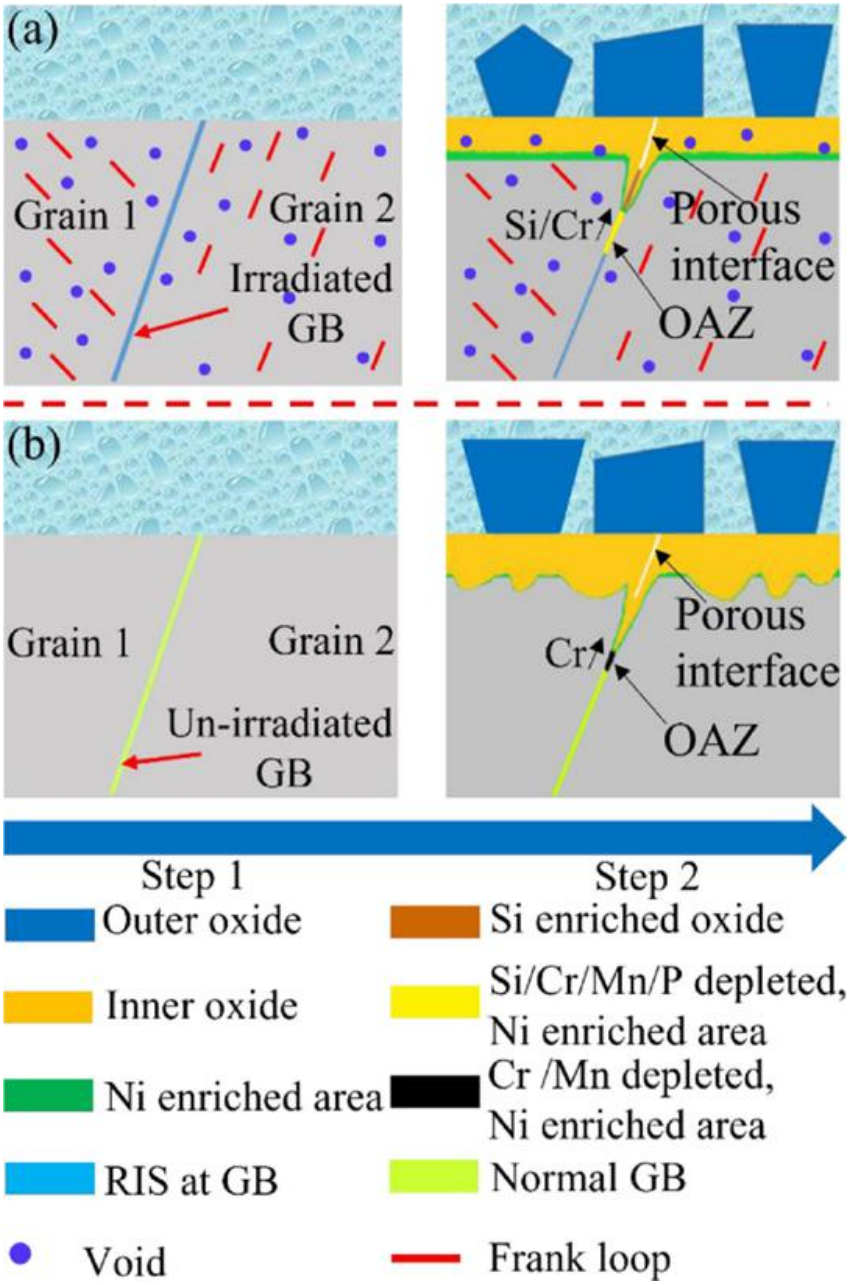


Fig. 10. Schematic showing the oxidation behavior at the grain boundaries of (a) irradiated and (b) unirradiated 316L exposed for 1000 h in the primary water environment of a simulated PWR [94].

In summary, irradiation segregation leads to Cr depletion and Ni and Si enrichment at the grain boundaries. However, its effect on the intergranular oxidation of materials remains unclear. In addition, the impact of RIS on intergranular corrosion has mostly been investigated at low radiation doses, but there is a lack of research at high radiation doses. Future studies should aim to strengthen our understanding of the mechanism of intergranular corrosion of materials at high radiation doses to bridge this research gap.

### 2.4.3 Effect of irradiation radiolysis on corrosion

Irradiation can directly affect material corrosion through irradiation damage, as described in detail in Sections 2.1 and 2.2. Furthermore, radiolysis can affect corrosive media. In PWRs, neutrons interact with the water coolant, leading to radiolysis (Equations (4) and (5)). This process results in the formation of long-lived molecules ($H_2$, $O_2$, and $H_2O_2$) and short-lived free radical substances ($H^{\cdot}$, $OH^{\cdot}$, $e^{-}_{aq}$, and $HO_2^{\bullet}$). These species can undergo oxidation ($O_2$, $H_2O_2$, $HO_2$) or reduction ($e^{-}_{aq}$, H, and $H_2$). Literature [101,107–111] provides a detailed review of the important reactions associated with these species and explains the charge conservation of $H^+$ and $OH^-$.

$$H_2O \xrightarrow{Ionizing\ radiation} e^{-}_{aq}, H^{\bullet}, HO^{\bullet}, HO_2^{\bullet} \quad \ldots \quad (4)$$

$$H_2O_2 \rightarrow O_2 + 2H^+ + 2e^- \quad (5)$$

The water radiolysis product $H_2O_2$ affects the electrochemical corrosion potential [108,110,111]. Figure 11 [112] shows the change in the corrosion potential of 304 and 316 stainless steels as a function of the $H_2O_2$ concentration. As the $H_2O_2$ concentration increases, the corrosion potential also increases until it reaches a saturation point. The saturated corrosion potential can extend to the penetration zone of the passivated film, where cracking/dissolution of the oxide film occurs [113-114]. When subjected to irradiation, the corrosion potential increases significantly. Was et al. [115,116] performed thermodynamic calculations and radiolysis modeling and found that at very high irradiation dose rates (4000 kGy/s), the corrosion potential increased by ~0.8$V_{SHE}$ compared to the unirradiated samples, thereby promoting material corrosion. In addition, in high-temperature water with low dissolved oxygen concentration and no dissolved hydrogen, the corrosion potential increased by more than 0.25$V_{SHE}$.

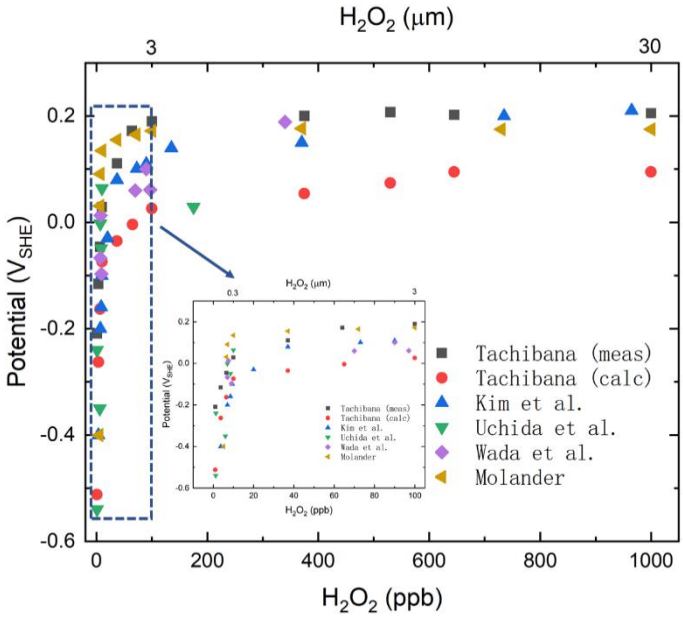


Fig. 11. Corrosion potential curve of 304 and 316 stainless steel as a function of the $H_2O_2$ concentration [112].

The characteristics of the oxides formed on the surface of the irradiated materials provide insight into the alteration of the stability of the species within the oxide film due to the irradiated environment. In experiments, the materials were irradiated with a proton beam and simultaneously exposed to a simulated PWR. Although radiolysis and irradiation damage occur on the surface of the materials simultaneously, in a series of experiments conducted by Was et al. [86,115,117], stainless steel samples not directly irradiated but exposed to radiolysis water exhibited oxide characteristics similar to those of the irradiated samples. Hematite was observed on the surface of the oxide, and Cr was deficient in the inner oxide layer, which differed from the oxide characteristics of the unirradiated sample. This indicated that water radiolysis was the primary mechanism affecting the properties and formation of the oxide. Comparing the oxides in the irradiated and unirradiated areas, such as the effect of irradiation-induced defects on corrosion, irradiation did not alter the double-layer structure of oxides formed on the material surface, which still consisted of an outer layer of oxide particles and an inner layer of a continuous oxide film. In situ irradiation corrosion experiments demonstrated significant changes in the morphology, composition, and depth of the inner oxide film compared to the unirradiated samples [88,115–119]. Using austenitic stainless steel as an example, the following observations were made:

- The oxides formed on the surfaces of the irradiated samples predominantly consisted of hematite and relatively few large planar oxide particles, primarily

consisting of densely packed small equiaxed crystals.

- The irradiated samples displayed a thinner and more porous inner oxide film with a lower Cr content, indicating the loss of Cr from the inner oxide layer after irradiation.

- The interface between the outer particles and the inner oxide was indistinct, and the metal/oxide interface fluctuated significantly in the irradiated samples.

As mentioned earlier, the long-lived radiolysis products ($H_2O_2$) generated by irradiation can significantly increase the corrosion potential. This alteration in the potential leads to the oxidation of $Fe^{2+}$ to $Fe^{3+}$ and the subsequent formation of hematite. Cr-rich spinel oxide dissolves to form $HCrO_4^-$ due to the increased corrosion potential. Consequently, the thickness of the inner oxide layer decreases, and Cr loss occurs. A lower Cr content indicates a less protective oxide film, leading to porosity. A higher diffusion rate of oxygen vacancies and cations due to worse protection by the inner scale results in further corrosion, contradicting the theory that the inner oxide layer is thinner. Hence, the growth of the inner oxide film on the irradiated alloy at a high-temperature and high-pressure water can be characterized as a competing process of solid oxidation and dissolution of the existing film.

## 3. Molten salt corrosion

### 3.1 Molten salt reactor environment

In a molten salt reactor (MSR), the operating temperature is usually higher than 700 ℃ and liquid fluoride serves as the coolant as well as the carrier for the nuclear fuel. This indicates that the structural materials are directly in contact with the molten fluoride salt. Consequently, the structural components face multiple harsh environmental challenges such as high temperatures, molten salt corrosion, and high-dose neutron irradiation [8]. The corrosion of the UNS N10003 alloy in pure molten salt is chiefly attributed to the selective dissolution of the active metal component, chromium (Cr) [120-124]. In addition, the complex chemical forms of lanthanides, actinides, impurities, and fission products present in the fuel salts accelerate the degradation of alloy performance and affect reactor safety [120-132]. The fission product, Te, diffuses into the UNS N10003 alloy, leading to embrittlement of the alloy under actual in-reactor service conditions [133,134]. The embrittlement failure of the alloy intensifies with increasing reactor power and Te concentrations [133-135].

During the operation of an MSR, the chemical form of uranium is extremely complex, especially the interaction between $U^{4+}/U^{3+}$ and specific components of the alloy through the reaction $2UF_4+Cr=CrF_2+2UF_3$, which affects the corrosion process [136].

### 3.2 Corrosion effect of the molten salt

Molten fluoride salt is an ideal coolant and nuclear fuel carrier in an MSR due to its favorable characteristics, including small neutron absorption cross-section, high-temperature stability, high thermal conductivity, high specific heat capacity, high boiling point, and low saturated vapor pressure. Ni-based and Fe-based alloys are considered potential structural materials that can be employed in molten fluoride salt reactors. Usually, these alloys undergo selective dissolution of the active alloying elements at the interface between the alloy and the molten salt. Unlike other high-temperature corrosive environments (such as supercritical water, air, and molten alloys), it is difficult for alloys in the molten salt systems to form a protective passive film on their surfaces to inhibit corrosion, primarily because oxides are unstable in molten salt environments. Thus, the mechanism of corrosion of alloys in molten salt environments can be microscopically manifested as the selective dissolution of active elements, mainly Cr, in Ni- and Fe-based alloys. The dissolution of Cr leads to the formation of vacancy defects near the interface and causes the internal Cr to diffuse toward the surface. This corrosion-induced loss of Cr results in a reduction of the alloy mass (corrosion weight loss). Furthermore, the accumulation of vacancy defects caused by corrosion leads to the formation of corrosion pits near the surface of the alloy [137]. As the corrosion time increases, both the size and the number of corrosion pits progressively increase.

In the 1950s, the Oak Ridge National Laboratory (ORNL) proposed using molten fluoride salt as a fuel system. Corrosion tests conducted on 18 different metal materials in 75 % NaF-25 % UF4 molten salt revealed that Ni alloys exhibited better resistance to molten salt corrosion compared to stainless steels [138]. Subsequently, compatibility with fluoride salts became a crucial criterion for selecting structural materials. From 1951 to 1952, ORNL conducted multiple static corrosion tests on various metallic materials, which demonstrated that loops made of stainless steel materials would be blocked. As a result, Ni-based Inconel 600 alloy was identified as a candidate material [139]. However, Inconel 600 also had the drawback of low strength. Hastelloy B, a Ni-Mo alloy with low chromium content, exhibited excellent strength and corrosion resistance against molten salt. Nevertheless, it posed challenges related to processing, oxidation, and stability [140]. Therefore, ORNL tried to develop a new

alloy based on the Hastelloy B alloying system. In a 1957 technical report (ORNL-2274), ORNL clearly pointed out that INOR-8 (i.e., UNS N10003 alloy, 70wt% Ni-16wt% Mo-7wt% Cr solution-strengthened Ni-based superalloy) met all design requirements. The UNS N10003 alloy was used as the main structural material in the molten salt experimental reactor (MSRE), which achieved criticality in 1965 and was decommissioned in 1969, making it the only alloy successfully employed in the MSR. [141,142].

Under ideal conditions, the UNS N10003 alloy exhibits general corrosion behavior. In the presence of moisture or oxidation impurities in the molten salt, the alloy is more prone to intergranular corrosion. The corrosion pattern observed for the molten salt is also related to the Cr content of the alloys. Alloys with high Cr content are more susceptible to intergranular corrosion than to general corrosion. Furthermore, the dissolution of Cr in alloys with a high Cr content is more pronounced. For example, corrosion pits in 316SS (with a Cr content of 18 %) and Inconel 617 (with a Cr content of 22 %) can be interconnected and penetrate through the material [124, 143]. For low-Cr alloys, such as UNS N10003 (Cr content 7 %), the corrosion pits generally remain isolated from one another, except in severe molten salt environments [124].

### 3.3 Driving force of molten salt corrosion

#### 3.3.1 Thermodynamic driving corrosion

The coolant salts used in an MSR typically consist of mixtures of alkali metal or alkaline earth metal fluorides such as LiF-NaF-KF or LiF-$BeF_2$. The driving force for molten salt corrosion originates from the difference in the Gibbs free energy between the molten fluoride salt and the metal fluoride. It is widely known that alkali metal (or alkaline earth metal) fluorides have the lowest Gibbs free energies among metal fluorides. Consequently, alloying elements, such as Cr, Fe, and Ni, cannot be chemically replaced by reactions in alkali metal (or alkaline earth metal) fluorides. Further, thermodynamic calculations indicate that the equilibrium concentrations of metals such as Ni, Mo, Co, Fe, and Cr in corrosion reactions involving LiF, NaF, KF, and $BeF_2$ are extremely low [144]. In general, when the equilibrium concentration of the reaction products is very low, it can be considered that the reaction does not occur. Therefore, the intrinsic corrosion of alloys containing these major elements in the impurity-free molten salt coolants is almost impossible. First-principles simulations and Molecular dynamics simulations have been used to investigate the thermodynamic properties of the molten salt. The results thus obtained reveal that the molten salt composition plays an important role in the corrosion of Ni-based alloys in

molten fluoride salts [145-147]. These studies help us to efficiently understand the basic fluorine-induced initial corrosion mechanism of Ni-based alloys in molten salt environments.

### 3.3.2 Impurity-driven corrosion

The impurities present in the molten salt are the main inducers of corrosion, especially in the initial stages, as shown in Fig.12. Oxidizing impurities ($H_2O$, HF, $NiF_2$, $FeF_2$, metal oxides, oxyacid ions, etc.) can act as oxidants in molten salts, leading to the rapid corrosion of alloys through various reaction mechanisms (Equations (6)–(10)) [120, 124]. However, as these impurities are consumed, the corrosion rate decreases, transitioning to a slower stage of corrosion.

$$H_2O(g) + 2MeF = M_2O + 2HF(g) \quad (6)$$

$$yHF(g) + xMe = Me_xF_y + \frac{1}{2}yH_2(g) \quad \text{(Me=Cr, Fe, Ni, Co, Al)} \quad (7)$$

$$FeF_2 + Cr = CrF_2 + Fe \quad 2FeF_3 + 3Cr = 3CrF_2 + 2Fe \quad (8)$$

$$NiF_2 + Cr = CrF_2 + Ni \quad 2CrF_2 + NiF_2 = 2CrF_3 + Ni \quad (9)$$

$$SO_4^{2-} + 2Cr = S + O^{2-} + Cr_2O_3 \quad (10)$$

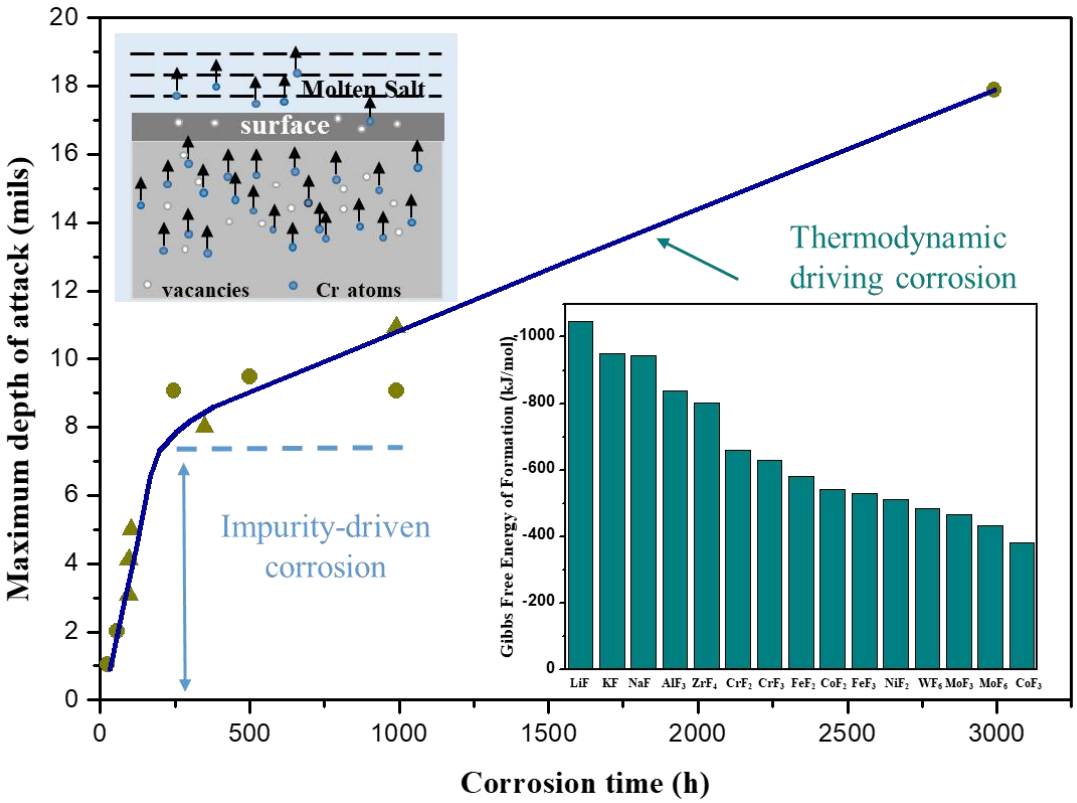


Fig. 12. Driving force of molten salt corrosion at different corrosion stages.

In the complex environment of nuclear reactors, the corrosion of alloys in molten salt environments is affected by multiple factors, including temperature differences [148,149], variations in the molten salt flow rate [150-152], presence of fission products [140-142], heterogeneous material corrosion (galvanic corrosion) [143,153-156], and irradiation-induced corrosion. In this paper, we focus on the effect of irradiation on the corrosion of alloys in molten salt environments and discuss the latest research progress.

### 3.4 Effect of irradiation on the corrosion of the molten salt

In nuclear reactors, irradiation damage can lead to the redistribution of atoms and the formation of defects in solids [157]. Compared to high-energy incident particles, the binding energy between lattice atoms is small (~10 – 60 eV). Thus, the incident particles can easily hit atoms (primary knock-on atoms, PKA) and displace them from their lattice position [157]. For example, when an elastic collision occurs, the primary colliding atom continues to collide elastically with the surrounding secondary colliding atoms, creating a irradiation time, interstitial atoms and vacancies accumulate and evolve into microscopic defects such as dislocation loops, cavities, bubbles, and stacking faults [75].

From a microstructural perspective, the irradiation as well as corrosion processes involve the movement and diffusion of atoms within the alloys. Irradiation damage enhances the migration and diffusion of atoms by introducing defects, such as helium and vacancies, within the alloy. These defects are displacement cascade, and eventually remaining at the interstitial atomic position, forming a Frank pair (interstitial atom and vacancy pair) [158]. With increasing one to being captured by interfaces, particularly grain boundaries, leading to the formation of helium bubbles or cavities and weakening of the properties of the interfaces [159]. Since the interfaces in alloys are important diffusion channels for elements [120], irradiation significantly affects the corrosion of alloys.

However, the synergistic effect of irradiation and molten salt corrosion on alloys is still a topic of debate. Previous tests on the UNS N10003 alloy in the MSRE program focused primarily on assessing the feasibility of the MSR and the usability of the alloy [160-163]. Although the mechanical properties of the UNS N10003 alloy under working conditions have been investigated, there are few reports on the microstructural changes in the alloy after neutron irradiation. Consequently, the mechanism underlying the synergistic effect of irradiation and molten salt corrosion on alloys remains unclear. However, in recent years, within the framework of the

fourth-generation nuclear reactors, such studies have gained wide attention. Ion irradiation techniques have been used to simulate the effect of neutron irradiation [80, 164], and shed light on the damage mechanisms of alloys in irradiated and corroded environments.

### 3.4.1 Helium bubbles

A critical problem for Ni-based alloys in an MSR is the accumulation of helium atoms [165,166]. The $^{59}$Ni nuclide in the Ni-based alloy has a very high (n, α) reaction cross-section, leading to the generation of a large amount of helium. Another important source of helium generating is the (n, α) reaction of thermal neutrons with $^{10}$B impurities in the alloy in the early stage of nuclear reactor operation. These He atoms can easily gather around the grain boundary to form He bubbles or cavities and cause intergranular fracture. This reduces the toughness of the alloy and its long-lasting life significantly, and results in the He brittleness of the alloy [167]. Thus, helium irradiation experiments were conducted on UNS N10003 alloy in a molten salt environment [168-173]. The results showed that helium irradiation accelerated the corrosion of the UNS N10003 alloy at a certain dose, at which obvious helium bubbles were observed via TEM characterization [171]. The presence of helium bubbles accelerated the corrosion of the UNS N10003 alloy in a molten salt environment in the following ways: 1) accelerating the dissolution of the alloying elements [168-160, 171, 174,175], 2) coarsening the surface of the alloy and enhancing intergranular corrosion [168], and 3) accelerating the formation of holes on the surface of the alloy [170,171].

An important mechanism by which helium bubbles accelerate the molten salt corrosion of alloys is the migration and diffusion of helium bubbles. Zhu et al. observed that the size of helium bubbles increased from 0.8 nm to 20 nm after the alloy was immersed in a molten salt environment. The migration of helium bubbles toward the interior bulk of the sample was observed, which coarsened the holes on the alloy surface and enhanced the intergranular corrosion of the UNS N10003 alloy [168]. Liu et al. reported the growth and coalescence of helium bubbles around the peak damaged region, which had no significant effect on the loss depth of Cr [170]. Lei et al. observed a unique outward migration of helium bubbles in a helium-ion-irradiated UNS N10003 alloy in a high-temperature molten salt environment, as shown in Fig.13. Helium bubbles can modify surface morphology and form holes through their outward migration. The formation of holes on the surface increases the contact area between the molten salt and the alloy, thus increasing the dissolution of Cr [171]. The dissolution of alloying elements also creates vacancies for the growth of helium

bubbles.

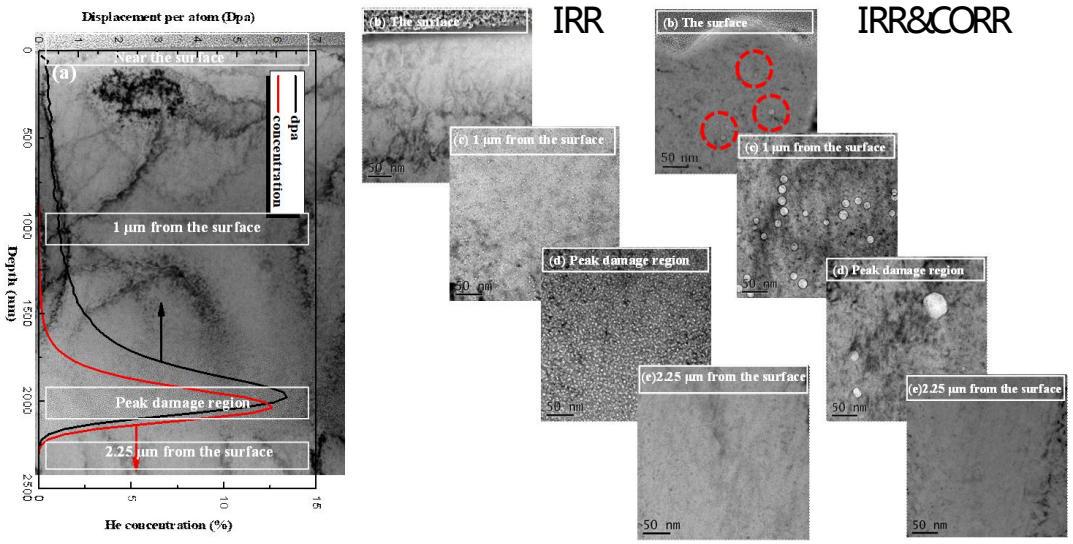


Fig. 13. Outward migration and growth of He bubbles from inside to the alloy surface after molten salt corrosion

Table 7. Experimental parameters in the studies of helium ion irradiation and molten salt corrosion

| Irradiation condition | | | Alloy | Corrosion condition | | | Ref. |
|---|---|---|---|---|---|---|---|
| Ions | Fluence | Temp. | | Molten salt | Time | Temp. | |
| 30keV He | ~1e17ion/cm$^2$ | RT | GH3535 | FLiNaK | 200h | 750 | [168] |
| 30keV He | ~1e17ion/cm$^2$ | RT | GH3535 | FLiNaK | 10\100\ 200h | 750 | [169] |
| 300keV He | 1e17ion/cm$^2$ | RT | welded GH3535 | FLiNaK | 400h | 700 | [170] |
| 1.2MeV He | 3e17ion/cm$^2$ | 650 | GH3535 | FLiNaK | 200h | 650 | [171, 172] |
| 2.2MeV He | 0.5/1.3e17ion/cm$^2$ | 700 | GH3535 Inconel 617 | FLiNaK | 50h | 700 | [173] |

### 3.4.2 Displacement damage defects

Fast neutrons in reactors cause displacement damage to the alloy through cascading collisions and form irradiation-induced defect clusters inside the alloy. These defect clusters strongly impede dislocation motion, resulting in the reduction of uniform elongation and fracture toughness of the alloy and inducing its hardening and

embrittlement. There is also evidence that displacement damage can influence the corrosion of alloys in molten salt environments.

Researchers from the Massachusetts Institute of Technology reported that irradiation can decelerate the intergranular corrosion of Ni-Cr alloys in molten salt via an in situ proton beam irradiation-molten salt corrosion experiment [176]. They attributed this inhibition to the self-healing of grain boundaries caused by the diffusion of Ni and Cr interstitial particles from proton irradiation. Irradiation introduces abundant interstitials into the alloys and enhances bulk diffusion. The diffusion of irradiation-induced interstitials to the grain boundary supplies dissolving atoms to the molten salt, thus decelerating the intergranular corrosion of the Ni-Cr alloys, as shown in Fig. 14. ORNL carried neutron irradiation- molten salt corrosion experiment on UNS N10003 alloy and 316SS alloy at 800 °C with an irradiation dose of $7.5\times10^{16}$ n/cm$^2$ [177]. The composition of the molten salt was NaCl-$MgCl_2$. The results of this study showed that neutron irradiation did not significantly affect the corrosion of the UNS N10003 alloy but decelerated the corrosion of the 316SS alloy. Helium ion irradiation can introduce helium bubbles into alloys, which can cause displacement damage. Researchers from Shanghai Institute of Applied Physics (SINAP) investigated the effect of helium ion irradiation with low and high ion fluences on the corrosion behavior of Inconel 617 and GH3535 alloys in FLiNaK molten salt at 700 °C [173]. For the substrates of both alloys, corrosion was observed to be accelerated with increasing irradiation doses. For the grain boundaries of the 617 alloy, the inhibition and promotion of intergranular corrosion were observed at low and high irradiation doses, respectively, which could be ascribed to the blocking of interstitial atoms, promotion of molten salt diffusion by helium bubbles, and self-healing mechanisms, as shown in Fig.15.

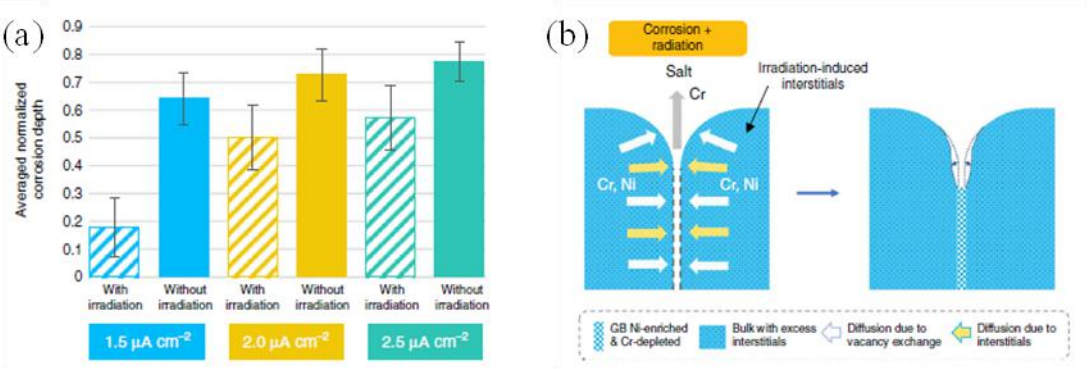


Fig. 14. Inhibition of corrosion of the NiCr alloy in FLiNaK salt following the in situ proton beam irradiation. (a) Corrosion depth of the alloy for different irradiation doses, and (b) schematic of the irradiation inhibition corrosion mechanism[176].

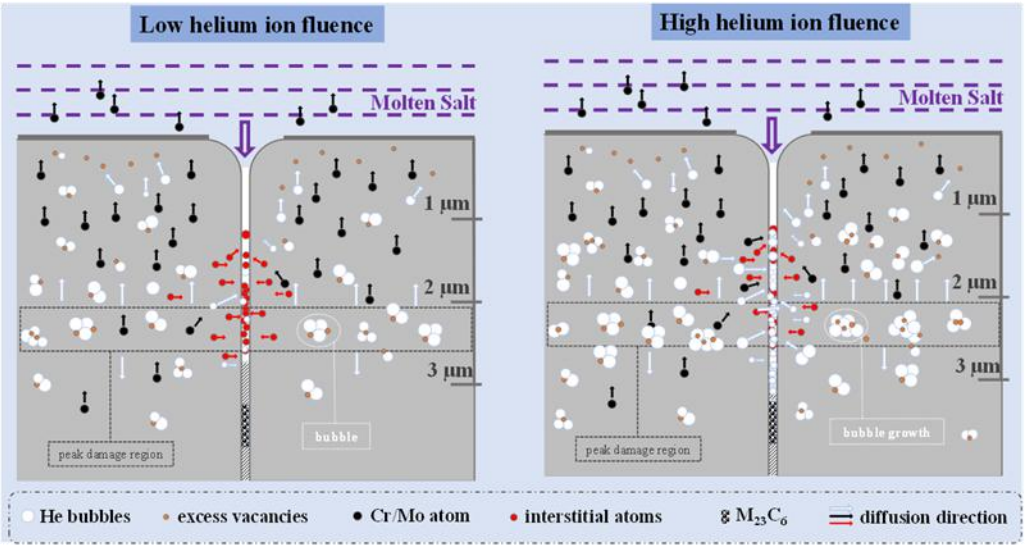


Fig. 15. Synergistic mechanism of irradiation and corrosion of Inconel 617 alloy [173]

Current studies have investigated the synergistic effects of neutron irradiation and corrosion, in situ and off-site ion irradiation, and corrosion. However, the selected alloys, irradiation temperatures, irradiation doses, and molten salt systems are all different. More experiments still need to be performed to clarify the effect of displacement damage on the molten salt corrosion of alloys.

### 3.4.3 RIS

Particle irradiation can induce element segregation and local microstructural changes in materials and is usually defined as RIS. During irradiation, point defects (vacancies and interstitial atoms) diffuse into nearby traps, such as the surface or internal grain boundaries of materials. Generally, the migration rates of these point defects differ. Some migrate to the sinks, whereas others remain away from them. Therefore RIS causes significant changes in the local composition of the material and affects its macroscopic properties.

RIS and precipitation are common in the pressure vessel steel of PWR. At low doses, the segregation of Cu, which leads to precipitation, can be observed by small-angle neutron scattering and scanning TEM (STEM). In addition, the segregation of Ni, Mn, P, Si, and other elements at dislocations or grain boundaries has also been reported [178]. In Cr-containing austenitic stainless steel and nickel-based alloys, irradiation-induced segregation leads to the diffusion of Cr to the grain boundaries, thus causing IASCC of the material. At lower temperatures, the concentration of defects increases, but they migrate to the sinks, leading to point-defect recombination. At higher temperatures, thermal diffusion is the dominant

mechanism, and the composition of the material tends to be uniform. In the intermediate temperature ($0.3–0.6T_m$), RIS is the most serious due to the "anti-Kirkendal effect." When the irradiation dose reaches 1–10 dpa, RIS can lead to local corrosion, grain boundary embrittlement, and a decline in the mechanical properties of the material. When the irradiation dose reaches 10 dpa, RIS leads to phase instability in the material, causing the generation of a new phase or decomposition of the existing phase [179]. In the Ni-Si system, when the solubility of Si in Ni reaches a certain degree, a new $Ni_3Si$ phase will be formed (γ' Phase) [180]. An RIS phenomenon was also observed in the alloy used for the MSR. Liu et al. and others used 30 keV Ar ions to irradiate a UNS N10003 alloy at room temperature. When the dose reached 48.4 dpa, a high concentration of Ni was observed at the grain boundary [181]. Huang et al. found that the precipitates rich in Mo and Cr appeared in the UNS N10003 alloy when the dose reached 10 dpa after Xe ion irradiation at 650 ℃ [182].

In a helium ion irradiated and molten salt corroded UNS N10003 alloy, Zhu et al. observed significant segregation of Si at the helium bubble surfaces, as shown in Fig. 16. When the segregation of Si increased to values above the solubility limit of ~ 10 at. % at the bubble surfaces [169], precipitation of a Ni-Si intermetallic compound occurs. The segregation of Si promotes chemical reactions between the Si atoms and the molten salt, thus enhancing localized corrosion damage. However, the formation of Ni-Si precipitates at large bubbles results in galvanic corrosion due to the difference in the electrochemical potentials between the Ni matrix and Ni-Si precipitates. Thus, RIS accelerates the localized corrosion damage of Ni-based alloys exposed to high-temperature molten salts.

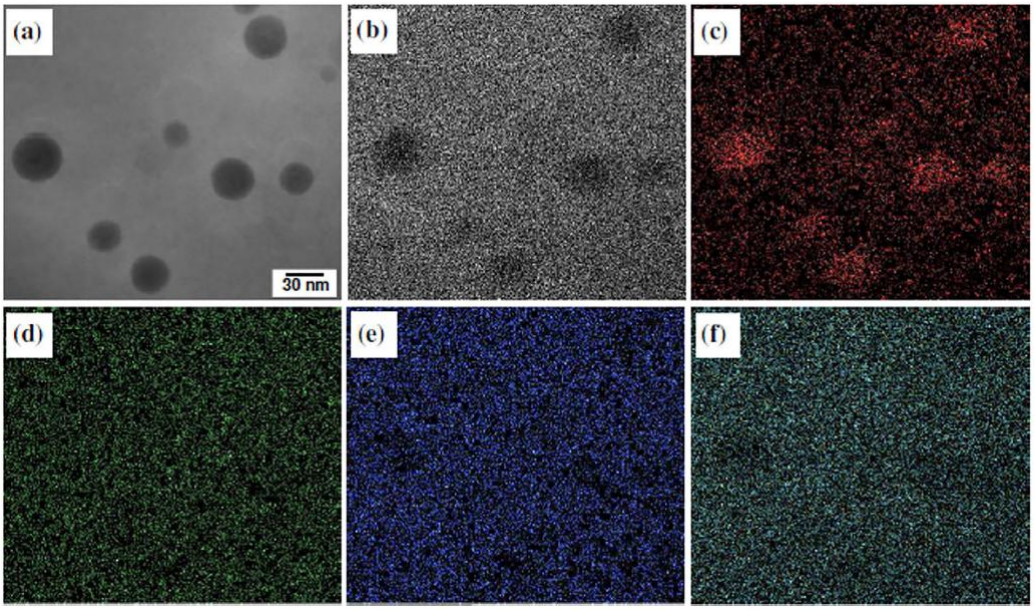


Fig. 16. Distribution of chemical elements in the uncorroded region of a sample irradiated and then corroded for 200 h: (a) High-angle annular dark-field imaging, and STEM-Energy dispersive X-ray spectroscopy (EDS) maps of (b) Ni, (c) Si, (d) Cr, (e) Mo, and (f) Fe [169].

### 3.4.4 Effects of the irradiation environment

In an MSR, the presence of fission products can significantly affect the corrosion of structural materials. The accumulation of fission products in the molten salt, resulting from the fission reactions in the core region, can interfere with the corrosion process and potentially promote corrosion due to the diffusion of specific fission products into the alloy. One such example is the deposition and diffusion of the fission product tellurium (Te) into the UNS N10003 alloy, which can lead to embrittlement of the grain boundaries of the alloy and potentially induce stress corrosion cracking. The extent of grain boundary embrittlement cracking caused by Te depends on the diffusion rate of Te in the alloy. In addition, the occurrence of Te-induced stress corrosion cracking at the grain boundaries is influenced by the concentration of Te and the applied stress load. [183-187].

These observations highlight the influence of Te concentration and applied stress on the susceptibility of the alloy to Te-induced stress corrosion cracking in a molten salt environment. Understanding these factors is crucial for designing corrosion-resistant structural materials and optimizing the operating conditions of the MSR.

## 4. Methods for inhibiting irradiation corrosion

Through a comprehensive review of recent studies on the effects of irradiation and corrosion on nuclear structural materials, it is not difficult to find that the effect of irradiation on corrosion can be categorized into two primary aspects. Firstly, irradiation-induced damage alters the microstructure of alloys by introducing Frankel pairs, impurity atoms, dislocations, voids, helium bubbles, and segregation of solute atoms. These changes can either promote or suppress the corrosion of alloys. Secondly, irradiation affects the corrosion of structural materials by altering the water or molten salt environments. In pressurized water reactors, the radiolysis of water produces oxidizing species, thereby accelerating corrosion. In MSRs, the fission product, Te, introduced by neutron irradiation is a significant factor that influences the corrosion of alloys. When Te in the fuel salt diffuses to the alloy surface, it forms tellurides, leading to intergranular cracking on the shallow surface of Hastelloy N alloy. ORNL modified Hastelloy N alloy by adding Nb and Ti to it in order to address the intergranular cracking induced by Te. Research has shown that Hastelloy N alloy modified with 1-2 % Nb exhibits favorable resistance to irradiation embrittlement and intergranular cracking caused by Te [188]. The addition of Nb improves the creep strength and fracture strain, of Hastelloy N while mitigating its embrittlement. When Nb or Ti is added to metal alloys, intergranular carbides are formed, which can capture helium atoms and impede their diffusion along the grain boundaries. Therefore, it is crucial to limit the addition of Ti and Nb to prevent the formation of the $Ni_3$ (Ti, Nb) phase. However, it is worth noting that when Ti is added, the effects of Cr and Nb are not significant [189].

Various strategies have been explored to enhance the irradiation and corrosion resistance of structural materials in PWRs and MSRs.

### 4.1 Surface treatment on the alloy to make the irradiation-resistant alloy resistant to corrosion

Material degradation processes such as corrosion, stress corrosion, wear, and fatigue cracking are frequently initiated at the material surface. Surface modification technologies, which involve altering the chemical composition and material microstructure near the surface of the material (typically ranging from one μm to several tens of μm) or applying a protective coating on the metal surface to mitigate the corrosion of structural materials, have garnered widespread attention in the field of material science. These protective layers can be fabricated by chemical or electrochemical processes. However, it is essential for the coating to possess good adhesion, uniformity, and coverage in order to provide effective protection to structural materials. In addition, the presence of cracks, resulting from the difference

in the coefficients of thermal expansion between materials, must be taken into consideration as even small cracks can lead to material corrosion.

Section 2.3 indicates that stainless steel has excellent corrosion resistance, mainly due to the formation of dense and continuous internal Cr-rich oxide films, such as $Cr_2O_3$. Cr is widely recognized as highly effective in safeguarding stainless steel and nickel-based alloys against corrosion in PWRs. Table 8 summarizes the advantages and disadvantages associated with several surface-coating technologies for obtaining Cr-rich coatings deposited on the metal surface to improve the corrosion resistance of the material.

Table 8. Examples of surface-coating technologies

| Approach | Advantages | Shortcoming |
|---|---|---|
| Thermal spraying [190,191] | 1. Wide applied area: a wide range of coating materials (such as ceramics, plastics, composite materials, and pure metal powders) can be applied on various substrates;<br>2. The coating thickness can be adjusted over a broad range, ranging from 15 μm to a few mm for substrates with large surface areas at high deposition rates;<br>3. Flexible process, workpieces of varying sizes, both large and small;<br>4. Excellent technical and economic efficiency, low operational difficulty, and low cost. | Defects, interlayers, high porosity, and low adhesion et al., occur in the coating. |
| Plasma source ion implantation [192-194] | 1. The surface properties can be selectively changed without altering the desired bulk material properties.<br>2. Eliminating concerns regarding bonding failure or delamination of the surface layers.<br>3. Good controllability and flexible process | Low injection efficiency, small area, and shallow depth;<br>The ion implantation system is complex and expensive. |
| Electrodeposition [195,196] | 1. The equipment is simple and easy to operate.<br>2. Low production costs under normal temperature and pressure conditions.<br>3. Electrodeposition can be performed on | The high stress inside the coating leads to warping and cracking of the coating |

| | | |
|---|---|---|
| | large and complex shaped parts.<br>4. Fast deposition rate. | |
| Laser-cladding technology [197] | High efficiency, low porosity, low dilution rate, small heat-affected zone, small deformation, and good combination | 1. The cost of this technique is high and the precision control is complex<br>2. Large-area coating is difficult |

In the conventional electroplating process, hexavalent Cr electrodeposition has been employed to deposit Cr-rich coatings onto metal surfaces. However, this deposition process generates highly toxic waste that poses a significant environmental hazard [195,196]. The thermal spraying process [190,191] is economical and simple. However, coatings produced with defects such as interlayers, high porosity, and low adhesion are not widely used to prepare complex structural coatings suitable for extreme environments. The laser cladding technology has been widely used in industries owing to its advantages of high efficiency, low porosity, and good adhesion. However, there are many defects in the coatings prepared by laser cladding. Therefore, to obtain a perfect coating using laser cladding, the process parameters must be adjusted repeatedly. Gu et al. [197] investigated the morphology, elemental distribution, electrochemical behavior, and oxidation resistance of 316L stainless steel with a Cr-rich coating prepared using the laser cladding method in a simulated PWR environment. Their findings revealed that the Cr-rich coating substantially improved the corrosion resistance of 316L stainless steel, with the best performance achieved by the Cr coating produced at 220 W.

In fluoride and chloride salt environment, the weight loss of the structural materials caused by corrosion is also related to the carbon content of the alloy. Carbide phases containing Cr formed at the grain boundaries provide favorable pathways for the diffusion and dissolution of Cr into the molten salt. Although it is known that Cr is preferentially corroded in fluoride salts, relatively high Cr and C contents are essential in traditional high-temperature alloys to maintain good high-temperature creep fracture strength and external oxidation resistance. Due to the excellent resistance to molten salt corrosion of pure nickel, Luke Olson et al. utilized 800H alloy as the substrate and applied a Ni-plating treatment with a thickness ranging from 40 μm to 180 μm [198], as shown in Fig. 17. Their experimental results indicated that Ni plating significantly improved the corrosion resistance of the 800H alloy in molten fluoride salts. During corrosion, Cr diffused from the alloy into the Ni-plated layer. However, if the Ni-plated layer was sufficiently thin, Cr eventually

dissolved into the molten salt. The microstructure of Ni-coating after corrosion, particularly the formation of voids, was also related to the thickness of the coating. The protective barrier effect of the Ni-plating was further enhanced by introducing a $Cr_2O_3$ barrier on the alloy surface before Ni-plating.

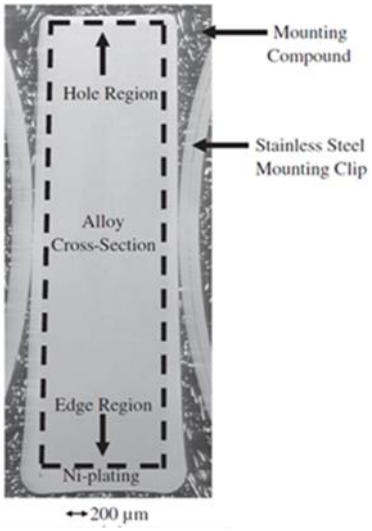


Fig. 17. SEM image photomontage of the cross-section of the Ni-plated Incoloy-800H showing variation in the thickness of Ni-plating.

**4. 2 Optimizing the corrosion-resistant alloy so that it resists irradiation**

Although the effect of irradiation on stainless steel or Ni-based alloys prepared by traditional processing remains a subject of debate, most studies have indicated that irradiation accelerates the corrosion of materials [19,20,83,87–90]. The material properties inevitably degrade over long-term irradiation corrosion under actual operational conditions. Consequently, there is significant interest in the field of nuclear energy in the development and fabrication of novel structural materials with superior radiation resistance to enhance their resistance to radiation-induced corrosion. Research and development efforts in radiation-resistant materials primarily fall into two categories: (1) High-entropy alloys (HEAs) with high-level lattice distortion and complex compositions can effectively alter the formation energy, migration barrier, and diffusion path of the irradiation-induced defects. This modulation enables the regulation of defect formation and recombination of interstitial vacancies during the early stage of irradiation [199–202]. (2) Nano-fine crystalline materials can be obtained or nano-precipitated particles can be introduced through thermal-mechanical processing and powder metallurgy, such as nano-layered metal composites [203,204] and oxide dispersion-strengthened (ODS) steel [205,206] nickel-based alloys [207-210]. In addition, the additive manufacturing technology allows the simultaneous generation

of submicron-scale (approximately 0.5 μm) cellular sub-crystalline structures and dispersed precipitates [211,212]. Oxide-matrix interfaces and cellular subgrain boundaries serve as defect sinks to absorb a large number of point defects (interstitial atoms and vacancies) generated during irradiation, thus improving the radiation resistance of the material.

HEAs have attracted significant attention as potential structural materials for advanced nuclear energy systems [213]. To date, studies that directly compare the irradiation and corrosion behavior of HEAs and other alloys have not been done. However, an interesting observation regarding the depth of the internal oxide films formed on the surface of the HEAs has emerged. Specifically, it has been noted that the depths of these films either remain unchanged or decrease following irradiation. Zhang et al. [79] first investigated the irradiation corrosion behavior of two novel HEAs, namely, $Mo_{0.5}NbTiVCr_{0.25}$ and $Mo_{0.5}NbTiVZr_{25}$, by subjecting them to irradiation with He ions followed by exposure to a simulated PWR for 200 h. Their results showed that irradiation up to 10.5 dpa had minimal impact on the composition, structure, and thickness of the oxide film formed on the surface of the $Mo_{0.5}NbTiVCr_{0.25}$ HEA. This phenomenon was primarily attributed to the excellent radiation resistance of HEA. At 10.5 dpa, the size of the dislocation ring and helium bubbles formed was small, exerting limited influence on the diffusion of oxygen and metal atoms. Furthermore, the presence of Ti, Nb, and Cr in the alloy promoted the formation of a highly protective oxide film. The thickness of the oxide film formed on the surface of the $Mo_{0.5}NbTiVZr_{25}$ HEA decreased after irradiation. A similar reduction in irradiation corrosion was also been observed in Zr-Nb alloy containing 1–2.5 % Nb, where Nb plays a role in reducing the irradiation corrosion rate.

Nanocrystalline materials, ODS steel, and alloys prepared by additive manufacturing technology exhibit a finer grain size and increased grain boundary density, which accelerates the diffusion of Cr. This leads to the formation of a thick Cr-rich film in the early stage of oxidation. This dense Cr-rich film acts as a protective layer, effectively inhibiting further oxidation. Liu et al. [77] compared the irradiation corrosion behavior of 304L stainless steel rolled using the traditional method and 304L stainless steel formed by selective laser melting (SLM). The SLM 304L exhibited relatively smaller oxide particles and a significantly thin inner oxide layer (116 ± 7.57 nm for the as-built sample, 166 ± 14.21 nm for the solution-annealed sample) in comparison to the traditionally rolled 304L stainless steel (348 ± 22.35 nm) after irradiation. Thus, SLM 304L stainless steel demonstrated a higher irradiation corrosion resistance when subjected to the simulated PWR primary water. This can be

attributed to the less irradiation-induced defects and the influence of its unique microstructure, which effectively mitigated corrosion. In addition, the corrosion resistance of ODS steel was observed to be influenced by the alloying elements and their contents. The appropriate combination of (14–16) Cr and (3.5–4.5) Al can efficiently improve the corrosion resistance of ODS steel in high-temperature and high-pressure water. Ren et al. [213] studied the corrosion of 16Cr-3Al ODS steel in supercritical water. After 1000 h of corrosion, the corrosion weight gain of the 16Cr-3Al ODS steel was substantially lower than that of the 9Cr ODS steel and stainless steel. The formation of dense $Al_2O_3$ was the main reason for the decreased corrosion rate of 16Cr-3Al ODS steel.

Carbide/oxide dispersion-strengthened (CDS/ODS) Ni-based alloys by incorporating nanoparticles into the alloy using powder metallurgy technology have successfully been developed [207-210]. Compared to SiC nanoparticles, $Y_2O_3$ nanoparticles exhibit smaller size, greater uniformity, and higher stability at high temperatures. This is due to the dissolution and reprecipitation processes that occur in these alloys. These characteristics provide a theoretical foundation for further improving the mechanical properties and resistance of alloys to He-induced damage. However, the presence of oxides can decrease the resistance of the alloys to molten salt corrosion. To verify this, a comprehensive study was conducted to examine the mechanical properties, irradiation performance, and molten salt corrosion resistance of ODS Ni-based alloys [214], as shown in Fig. 18. The results obtained from this study show that compared to the Hastelloy N alloy, the ODS Ni-based alloy has better tensile strength, yield strength, and resistance to swelling caused by helium bubbles. In addition, the alloy exhibits excellent resistance to molten salt corrosion, highlighting its significant potential as a core component material in MSRs.

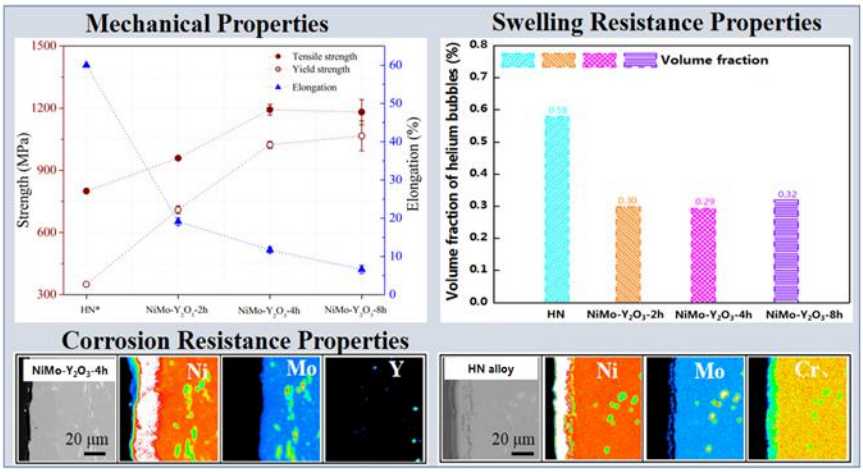


Fig. 18. Mechanical, irradiation, and corrosion properties of NiMo-$Y_2O_3$ alloy.

### 4.3 Adjusting the corrosion potential of water and molten salt to slow down the corrosion of the alloy

The two dominant methods for controlling corrosion in PWRs are Zn injection and dissolved hydrogen optimization. Zn injection was applied to the primary coolant system of PWRs, in the US 1990s [215], to reduce the irradiation dose [215]. Zn injection promotes the formation of thinner and more protective oxides on stainless steel and alloy 600, with Zn substitution in the spinel-type oxide forming the stable $ZnCr_2O_4$ compound [216-219]. Furthermore, Zn injection has been found to alleviate the degradation of the primary water stress corrosion cracking (PWSCC) in PWRs. This can be attributed to Zn inhibiting the initiation of cracking [220] and reducing the crack growth rate (CGR) [31,219]. The main reason for the inhibition of PWSCC is that Zn injection delays the initiation of stress corrosion cracks. Extensive laboratory data supports a reduction of 2–10 times in crack initiation and approximately 1.5 times in CGR [31].

In the primary water in a PWR, an oxidant is generated and the corrosion potential moves forward due to radiation-induced water radiolysis, which leads to an increase in the corrosion rate, as described in Section 2.4.3. Hydrogen gas is injected into the water supply system to prevent the accumulation of oxidant products such as oxygen and hydrogen peroxide and to reduce the corrosion potential of the alloy, thus efficiently suppressing water radiolysis. $H_2$ recombines with $H^{\bullet}$, $HO^{\bullet}$, and $H_2O_2$ and transforms them back into water through the following chain reaction [107]:

$$H_2 + HO^{\bullet} \rightarrow H^{\bullet} + H_2O$$

$$H^{\bullet} + H_2O_2 \rightarrow HO^{\bullet} + H_2O$$

$$H_2 + H_2O_2 \rightarrow 2H_2O$$

Some studies [59, 63, 221–223] have provided evidence to support the observation that the corrosion potential and corrosion rate of Ni-based alloys decrease as the concentration of dissolved hydrogen increases in the simulated PWR primary water. Fig. 19 illustrates the thickness of the oxide films in the simulated primary water with various DH concentrations. In addition, the Cr concentration increases, whereas the Ni concentration decreases with higher levels of DH. DH weakens the stability and protection of the Ni spinel oxide films, and the susceptibility of Ni-based alloys to PWSCC reaches its peak in the vicinity of the Ni/NiO phase transition. To effectively

delay the crack-initiation time and reduce the susceptibility to PWSCC, it is crucial to maintain a low DH concentration within the stable NiO region.

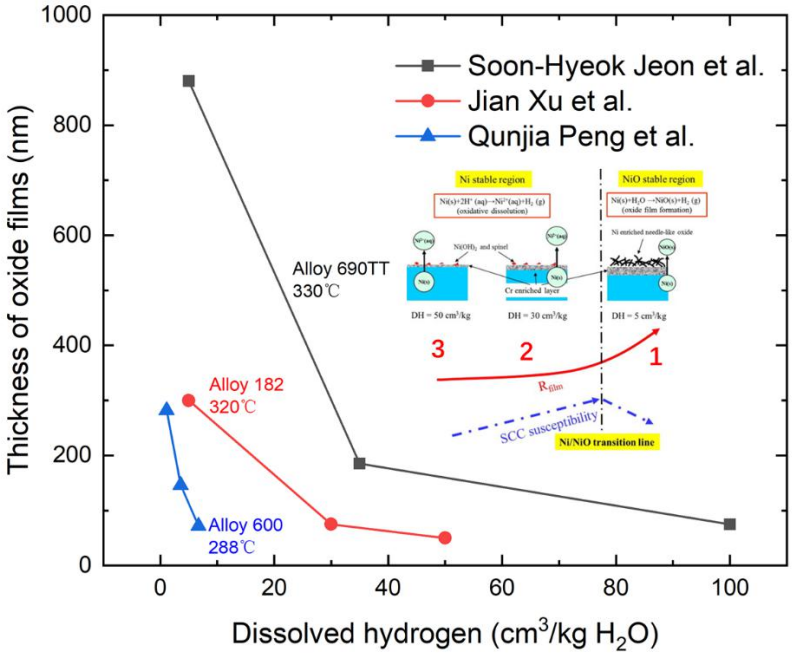


Fig. 19. Thickness of oxide films in the simulated primary water as a function of DH concentration. The illustration in the inset shows the schematic of the oxide film formed on alloy 182 at the dissolution H value on the red broken line [59,63,221].

Only limited research [30,33,224] has been conducted on the effect of DH concentration on the corrosion of stainless steel in high-temperature water. In the study by Takumi et al., it was observed that increasing the DH slightly elevated the corrosion rate [33]. However, the opposite conclusion was drawn in the study by Dong et al. [224], who found that the oxide film on 316L SS was thinner in hydrogenated PWR water than in deuterated PWR water. Investigations are thus necessary to optimize the hydrogen content and increase corrosion resistance.

The addition of redox agents to molten salt can affect the corrosion potential of the salt, thereby decreasing the corrosion rate of the alloy. Corrosion is an irreversible electrochemical process that occurs until an equilibrium is reached. Therefore, from a dynamic perspective, it is important to consider the effect of redox control on metal corrosion. Most oxidants in the salt are consumed by redox reactions. In other words, the reducing agent acts as a sacrificial material protecting the metal. Redox control can be achieved through gas-phase control (e.g., $HF/H_2$), major metal control (e.g., Be (II)/Be), and dissolved salt control (e.g., U (IV)/U (III)) [225].

Research conducted at ORNL studied the corrosion rate of stainless steel in FLiBe salts with and without beryllium metal. Without adding beryllium metal to the molten salt, the corrosion rate of 316 SS was approximately 8 μm/year after 3000 h of corrosion. The weight loss initially decreased rapidly within the first 1000 h, possibly due to the impurities present in the salt, and the subsequent corrosion was driven by thermal gradients. In contrast, the corrosion rate significantly decreased to less than 2 μm/year when beryllium was added to the molten salt [226].

The content of $UF_4$ not only influences the corrosion potential of the salt but also affects the structure of the molten salt. Bessada et al. reported that the structure of the molten salt can be rearranged by adding a few moles of $UF_4$ to the mixture to increase the basicity of the molten salts. This indicates that changing the structure of the molten salt would suppress its corrosion [227]. In addition to the experimental approaches, a combination of the extended X-ray absorption fine structure (EXAFS) and molecular dynamics simulations have proven to be valuable tools for exploring the structure of molten salts and the rich chemistry of the molten salt systems.

With regards to the fission products, Te induces corrosion. Some studies have shown that Te embrittlement can be mitigated by reducing the oxidation-reduction potential of the salts. To achieve this, the activity ratio of the tetravalent to trivalent uranium ions in the salt can be adjusted. Although the oxidation-reduction potential can be adjusted to reduce the oxidizability of the salt (e.g., by exposing the salt to Be or Cr), the activity of $UF_3$ in the salt must be sufficiently low to avoid its disproportionation and alloying of uranium with the containment alloy [228].

Various studies have also focused on improving the resistance of alloys to Te embrittlement. One approach involves the addition of trace elements to the alloy to form nanoprecipitates, which can decrease the influence of Te and hinder the diffusion of Te atoms. Han et al. investigated the effect of Te vapor on the intergranular embrittlement of a Y-modified Ni-16Mo-7Cr-based alloy at 800 °C. Their results indicated that the addition of Y significantly reduced the diffusion depth of Te in the alloy, thus improving its resistance to intergranular cracking [229]. The YTe phase near the surface reaction layer and surface grain boundaries plays an important role in fixing and decreasing the diffusion of Te. The presence of the YTe phase near the surface reaction layer and the surface grain boundaries plays a crucial role in immobilizing Te and retarding its diffusion. The segregation of Y from the substrate to the surface and the formation of the YTe phase in the reaction layer and grain boundaries are the main factors contributing to the reduced diffusion depth of Te in the Y-modified alloy. The diffusion depth of Te in the Y-modified alloy is ~40 μm,

whereas it exceeds ~70 μm in the GH3535 alloy. However, adding more than 0.05 wt% Y to the alloy does not consistently improve its intergranular brittleness and may even degrade its mechanical properties.

The addition of La also efficiently reduces the diffusion depth of Te in the alloy, thus decreasing its susceptibility to intergranular cracking [230]. Although $LaTe_3$ has not been observed during the interaction between Te and the alloy, the segregation of La in the surface telluride reaction layer and the presence of the $LaNi_5$ intermetallic compound at the grain boundaries facilitate the formation of NiTe, which contributes to the reduced diffusion depth of Te in the La-modified alloys. The optimal concentration of La in the alloy should be approximately 0.1 wt%. Excessive La concentration can lead to an increase in the formation of the $LaNi_5$ phase, which will not improve the mechanical properties of the alloy. In addition, the crack resistance of the intergranular alloys does not increase with increasing La concentration.

Overall, breakthroughs in material science, ranging from material development to performance evaluation, are extremely challenging. These challenges require extensive testing and in-depth research on structural materials, particularly on the construction and development of equipment that closely simulates the real working conditions for in situ research. In addition to experimental testing, theoretical calculations and modeling at various scales, ranging from atomic to grain levels, will contribute significantly to our profound understanding of material behavior under multiple environmental conditions [231]. Furthermore, the integration of new alloy and microstructure design methodologies with novel material processing and manufacturing technologies is crucial for achieving optimal system performance under demanding operating conditions.

## 5. Conclusion and outlook

The service behavior of the structural materials of reactors under operating conditions is a key factor that affects the life of the reactor, and understanding the synergistic effects of irradiation and corrosion on these materials is a challenging research area. This review focuses on the effects of irradiation on the corrosion properties of structural materials in PWRs and MSRs, and highlights the following main conclusions:

Austenitic stainless steel and Ni-based alloys are the key structural materials for the core of PWRs. Their corrosion behavior in high-temperature and high-pressure water environments is closely associated with the formation of oxides on the alloy

surface. The formation of an oxide is a product of the interaction between the alloy elements and the water medium, and is also a key factor affecting the process of IASCC. Therefore, this study introduces the morphology and structure of the oxide, along with the mechanisms governing its formation and growth. This review summarizes the effect of irradiation on general corrosion behavior and intergranular oxidation of alloys, and highlights three key aspects:

1) The effect of irradiation-induced defects on the corrosion rate of the alloys depends on the size of the defects.

2) The presence of Cr improves the corrosion resistance of the alloy by forming a dense protective film on its surface. Irradiation-induced sputtering leads to the formation of a thin Cr-rich oxide layer on the surface of the alloy, thus efficiently mitigating the initial corrosion. However, RIS of Cr at the grain boundaries results in the depletion of Cr, thereby accelerating grain boundary corrosion and cracking. The preferential diffusion of Si at the grain boundaries creates vacancies for oxides located at the grain boundaries, promoting the enrichment of Cr in the oxides and thus enhancing the intergranular corrosion resistance of the alloy.

3) Radiolysis increases the corrosion potential and accelerates the overall corrosion process.

In MSRs, the structural material primarily consists of Ni-based alloys that cannot form a protective passive film in the molten salt environment. The corrosion mechanism of these alloys is primarily attributed to the selective dissolution of the active elements. In the early stages of corrosion, the corrosion of the alloy is significantly affected by the impurities in the molten salt. When the impurities are depleted, corrosion is primarily driven by thermodynamics. Irradiation can affect the molten salt corrosion of Ni-based alloys via various mechanisms as listed below:

1) Irradiation-induced defects accelerate the diffusion process, leading to an increased corrosion rate of the alloy.

2) The corrosion of the grain boundaries of the alloy is influenced by three effects: blockage, diffusion, and self-healing of the interstitial atoms.

3) RIS increases the chemical reactivity of the alloy elements with molten salts, enhancing the galvanic effect and promoting alloy corrosion.

4) Fission products and fuel introduced by irradiation can also affect the corrosion of alloys.

Considering the factors influencing the irradiation and corrosion performance of structural materials in PWRs and MSRs, several strategies have been proposed to mitigate their corrosion: (i) implementing protective measures for irradiation-resistant alloys, such as enhancing the corrosion resistance of the surface coatings to slow down the corrosion rate, (ii) developing new materials with improved irradiation and corrosion resistance, and (iii) reducing the oxidation-reduction potential of water and molten salt medium, which is also an effective way to decreasing the corrosion rate.

Overall, in order to ensure the safe operation of reactors, it is important to study the service behavior of materials and grasp the evolution laws of material properties under the combined effects of irradiation and high-temperature corrosion operating environment of the reactors. Further theoretical and in situ experimental work is necessary to deepen our understanding of the relevant mechanisms and develop optimized solutions.

**Acknowledgments**

This work was supported by the National Natural Science Foundation of China (Grant Nos. 12022515 and 11975304), and the Youth Innovation Promotion Association, Chinese Academy of Sciences (Grant No. Y202063).

**Data availability**

This is a review paper, and all data is based on published literatures, which can be obtained from the internet without any data acquisition issues.

**References**

[1] G.S. Was, P.L. Andresen, in *Nuclear Corrosion Science and Engineering*, ed. by D. Féron (Elsevier, Netherland, 2012), pp. 131-185

[2] F. Vaillant, T. Couvant, J.M. Boursier, et al., Stress Corrosion Cracking of Cold Worked Austenitic Stainless Steels in Laboratory Primary PWR Environment. Paper presented at Pressure Vessels and Piping Conference, San Diego, California, USA, 25-29 July 2004

[3] T. Couvant, L. Legras, C. Pokor, et al., Investigations on the mechanisms of PWSCC of strain hardened austenitic stainless steels. Paper presented at the 13th International conference on environmental degradation of materials in nuclear power systems, Whistler, Canada, 19-23 Aug 2007

[4] P. Huguenin, F. Vaillant, T. Couvant, et al., EDF program on SCC initiation of cold-worked stainless steels in primary water. Paper presented at the European Corrosion Congress. Corrosion from the nano scale to the plant, Nice, France, 6-10

Sep 2009
[5] D.M. Wright, Dissertation, University of Manchester, 2012
[6] R. Hosler, S. Fyfitch, H. Malikowski, et al., Review of stress corrosion cracking of pressure boundary stainless steel in pressurized water reactors and the need for long-term industry guidance. Paper presented at International Conference on Environmental Degradation of Materials in Nuclear Power Systems-Water Reactors, Asheville, North Carolina, USA, 2016
[7] International Atomic Energy Agency. (Nuclear Technology Review Report, Austria: IAEA, 2018)
[8] H.E. McCoy, Status of materials development for molten salt reactors (Oak Ridge National Laboratory, Oak Ridge, 1978)
[9] T. Allen, J. Busby, M. Meyer, et al., Materials challenges for nuclear systems. Mater. Today **13**, 14-23 (2010). doi:10.1016/S1369-7021(10)70220-0
[10] S.J. Zinkle, G.S. Was, Materials challenges in nuclear energy. Acta Mater. **61**, 735-758 (2013). doi:10.1016/j.actamat.2012.11.004
[11] G.S. Was, S.M. Bruemmer, Effects of irradiation on intergranular stress corrosion cracking. J. Nucl. Mater. **216**, 326-347 (1994). doi:10.1016/0022-3115(94)90019-1
[12] E.P. Simonen, S.M. Bruemmer, Radiation effects on environmental cracking of stainless steels. JOM **50**, 52-55 (1998). doi:10.1007/s11837-998-0309-3
[13] C.F. Cheng, Intergranular stress-assisted corrosion cracking of austenitic alloys in water-cooled nuclear reactors. J. Nucl. Mater. **57**, 11-33 (1975). doi:10.1016/0022-3115(75)90175-0
[14] P. Scott, A review of irradiation assisted stress corrosion cracking. J. Nucl. Mater. **211**, 101-122 (1994). doi:10.1016/0022-3115(94)90360-3
87
[15] S.M. Bruemmer, E.P. Simonen, P.M. Scott, et al., Radiation-induced material changes and susceptibility to intergranular failure of light-water-reactor core internals. J. Nucl. Mater. **274**, 299-314 (1999). doi:10.1016/S0022-3115(99)00075-6
[16] S.M. Bnlemmer, B.W. Arey, L.A. Chariot, in Grain Boundary Chromium Concentration Effects on the IGSCC and IASCC of Austenitic Stainless Steels (Pacific Northwest National Laboratory, Richland, 1993)
[17] A.J. Jacobs, G.P. Wozadlo, Irradiation-assisted stress corrosion cracking as a factor in nuclear power plant aging. J. Mater. Eng. **9**, 345-351 (1988). doi:10.1007/bf02834045
[18] T. Shoji, S.I. Suzuki, K.S. Raja, Current status and future of IASCC research. J. Nucl. Mater. **258-263**, 241-251 (1998). doi:10.1016/S0022-3115(98)00304-3
[19] M. Boisson, L. Legras, E. Andrieu, et al., Role of irradiation and irradiation

defects on the oxidation first stages of a 316L austenitic stainless steel. Corros. Sci. **161**, 108194 (2019). doi:10.1016/j.corsci.2019.108194
[20] P. Deng, Q.J. Peng, E.H. Han, et al., Effect of irradiation on corrosion of 304 nuclear grade stainless steel in simulated PWR primary water. Corros. Sci. **127**, 91-100 (2017). doi:10.1016/j.corsci.2017.08.010
[21] Z. Jiao, G. Was, in Proceedings of 15th International Conference on Environmental Degradation of Materials in Nuclear Power Systems - Water Reactors, ed. by J.T. Busby, G. Ilevbare, P.L. Andresen. The Minerals, Metals & Materials Society (Springer, Cham, 2011), p. 1329-1338
[22] Z. Jiao, J.T. Busby, G.S. Was, Deformation microstructure of proton-irradiated stainless steels. J. Nucl. Mater. **361**, 218-227 (2007). doi: 10.1016/j.jnucmat.2006.12.012
[23] T. Onchi, K. Dohi, N. Soneda, et al., Mechanism of irradiation assisted stress corrosion crack initiation in thermally sensitized 304 stainless steel. J. Nucl. Mater. **340**, 219-236 (2005). doi:10.1016/j.jnucmat.2004.11.012
[24] Z. Jiao, G.S. Was, Localized deformation and IASCC initiation in austenitic stainless steels. J. Nucl. Mater. **382**, 203-209 (2008). doi:10.1016/j.jnucmat.2008.08.032
[25] T. Couvant, in *Materials Ageing and Degradation in Light Water Reactors: Mechanisms and Management*, ed. by K.L. Murty (Elsevier, Netherland, 2013), pp. 70-80
[26] Y. Wouters, L. Latu-Romain, in *Encyclopedia of Interfacial Chemistry, Surface Science and Electrochemistry*, ed. by K. Wandelt (Elsevier, Netherland, 2018), pp. 155-163
[27] M. Le Calvar, I. De Curières, in *Nuclear Corrosion Science and Engineering*, ed. by D. Féron (Elsevier, Netherland, 2012), pp. 473-547
[28] M.L. Castao, B.V.D. Schaaf, A. Roth, et al., in EUROCORR 2004 - Prevision a long terme et modelisation de la corrosion, Nice, France, 12-16 Sep 2004
[29] J.J. Chen, Q. Xiao, Z.P. Lu, et al., Characterization of interfacial reactions and oxide films on 316L stainless steel in various simulated PWR primary water environments. J. Nucl. Mater. **489**, 137-149 (2017). doi:10.1016/j.jnucmat.2017.03.029
[30] X.Y. Zhong, S. Xia, J. Xu, et al., The oxidation behavior of 316L in simulated pressurized water reactor environments with cyclically changing concentrations of dissolved oxygen and hydrogen. J. Nucl. Mater. **511**, 417-427 (2018). doi:10.1016/j.jnucmat.2018.09.049
[31] O.K. Chopra, A.S. Rao, A review of irradiation effects on LWR core internal

materials - IASCC susceptibility and crack growth rates of austenitic stainless steels. J. Nucl. Mater. **409**, 235-256 (2011). doi:10.1016/j.jnucmat.2011.02.059

[32] P.M. Scott, P. Combrade, General corrosion and stress corrosion cracking of Alloy 600 in light water reactor primary coolants. J. Nucl. Mater. **524**, 340-375 (2019). doi: 10.1016/j.jnucmat.2019.04.023

[33] C.J. Wood, *Comprehensive Nuclear Materials* (Elsevier, Netherland, 2012), pp. 17-47

[34] K. Kruska, S. Lozano-Perez, D.W. Saxey, et al., Nanoscale characterisation of grain boundary oxidation in cold-worked stainless steels. Corros. Sci. **63**, 225-233 (2012). doi:10.1016/j.corsci.2012.06.030

[35] T. Terachi, T. Yamada, T. Miyamoto, et al., Corrosion behavior of stainless steels in simulated PWR primary water-effect of chromium content in alloys and dissolved hydrogen-. J. Nucl. Sci. Technol. **45**, 975-984 (2008). doi:10.1080/18811248.2008.9711883

[36] S. Cissé, L. Laffont, B. Tanguy, et al., Effect of surface preparation on the corrosion of austenitic stainless steel 304L in high temperature steam and simulated PWR primary water. Corros. Sci. **56**, 209-216 (2012). doi:10.1016/j.corsci.2011.12.007

[37] R.L. Tapping, R.D. Davidson, E. Mcalpine, et al., The composition and morphology of oxide films formed on type 304 stainless steel in lithiated high temperature water. Corros. Sci. **26**, 563-576 (1986). doi:10.1016/0010-938X(86)90024-7

[38] T. Terachi, K. Fujii, K. Arioka, Microstructural characterization of scc crack tip and oxide film for SUS 316 stainless steel in simulated PWR primary water at 320°C. J. Nucl. Sci. Technol. **42**, 225-232 (2005). doi:10.1080/18811248.2005.9726383

[39] B. Stellwag, The mechanism of oxide film formation on austenitic stainless steels in high temperature water. Corros. Sci. **40**, 337-370 (1998). doi:10.1016/S0010-938X(97)00140-6

[40] S.E. Ziemniak, M. Hanson, Corrosion behavior of 304 stainless steel in high temperature, hydrogenated water. Corros. Sci. **44**, 2209-2230 (2002). doi:10.1016/S0010-938X(02)00004-5

[41] M.D.C. Belo, M. Walls, N.E. Hakiki, et al., Composition, structure and properties of the oxide films formed on the stainless steel 316L in a primary type PWR environment. Corros. Sci. **40**, 447-463 (1998). doi:10.1016/S0010-938X(97)00158-3

[42] R. Soulas, M. Cheynet, E. Rauch, et al., TEM investigations of the oxide layers formed on a 316L alloy in simulated PWR environment. J. Mater. Sci. **48**, 2861-2871 (2013). doi:10.1007/s10853-012-6975-0

[43] Z. Szklarska-Smialowska, K.C. Chou, Z.Z. Xia, The composition and properties of oxide films on type 304 stainless steel on exposure to lithiated water at 100–350°C. Corros. Sci. **32**, 609-619 (1991). doi:10.1016/0010-938X(91)90110-B

[44] G. Hultquist, C. Leygraf, The initiation of selective oxidation of a ferritic stainless steel at low temperatures and oxygen pressures. Corros. Sci. **22**, 331-346 (1982). doi:10.1016/0010-938X(82)90034-8

[45] J. Robertson, The mechanism of high temperature aqueous corrosion of stainless steels. Corros. Sci. **32**, 443-456 (1991). doi:10.1016/0010-938X(91)90125-9

[46] J. Ensling, J. Fleisch, R. Grimm, et al., A corrosion study of austenitic and martensitic steels under boiler conditions by means of $^{57}$Fe conversion electron mössbauer spectroscopy. Corros. Sci. **18**, 797-804 (1978). doi:10.1016/0010-938X(78)90016-1

[47] M. Dumerval, S. Perrin, L. Marchetti, et al., Hydrogen absorption associated with the corrosion mechanism of 316L stainless steels in primary medium of Pressurized Water Reactor (PWR). Corros. Sci. **85**, 251-257 (2014). doi:10.1016/j.corsci.2014.04.025

[48] M. Sennour, L. Marchetti, F. Martin, et al., A detailed TEM and SEM study of Ni-base alloys oxide scales formed in primary conditions of pressurized water reactor. J. Nucl. Mater. **402**, 147-156 (2010). doi:10.1016/j.jnucmat.2010.05.010

[49] L. Marchetti, S. Perrin, O. Raquet, Corrosion mechanisms of Ni-base alloys in pressurized water reactor primary conditions, Mater. Sci. Forum **595**, 529-537 (2008). doi:10.4028/www.scientific.net/MSF.595-598.529

[50] A. Machet, A. Galtayries, S. Zanna, et al., XPS and STM study of the growth and structure of passive films in high temperature water on a nickel-base alloy. Electrochim. Acta **49**, 3957-3964 (2004). doi:10.1016/j.electacta.2004.04.032

[51] L. Marchetti, S. Perrin, F. Jambon, et al., Corrosion of nickel-base alloys in primary medium of pressurized water reactors: New insights on the oxide growth mechanisms and kinetic modelling. Corros. Sci. **102**, 24-35 (2016). doi:10.1016/j.corsci.2015.09.001

[52] F. Carrette, M.C. Lafont, L. Legras, et al., Analysis and TEM examinations of corrosion scales grown on alloy 690 exposed to PWR environment. Mater. High Temp. **20**, 581-591 (2014). doi:10.1179/mht.2003.067

[53] J. Panter, B. Viguier, J.M. Cloué, et al., Influence of oxide films on primary water stress corrosion cracking initiation of alloy 600. J. Nucl. Mater. **348**, 213-221 (2006). doi:10.1016/j.jnucmat.2005.10.002

[54] F. Delabrouille, B. Viguier, L. Legras, et al., Effect of the chromium content on the corrosion of nickel based alloys in primary water of pressurised nuclear reactors.

Mater. High Temp. **22**, 287-292 (2005). doi:10.1179/mht.2005.033
[55] C.O.A. Olsson, D. Landolt, Passive films on stainless steels - Chemistry, structure and growth. Electrochim. Acta **48**, 1093-1104 (2003). doi:10.1016/S0013-4686(02)00841-1
[56] H. Sun, X.Q. Wu, E.H. Han, et al., Effects of pH and dissolved oxygen on electrochemical behavior and oxide films of 304SS in borated and lithiated high temperature water. Corros. Sci. **59**, 334-342 (2012). doi:10.1016/j.corsci.2012.03.022
[57] X.H. Liu, X.Q. Wu, E.H. Han, Effect of Zn injection on established surface oxide films on 316L stainless steel in borated and lithiated high temperature water, Corros. Sci. **65**, 136-144 (2012). doi:10.1016/j.corsci.2012.08.022
[58] Y.B. Qiu, T. Shoji, Z.P. Lu, Effect of dissolved hydrogen on the electrochemical behaviour of Alloy 600 in simulated PWR primary water at 290 °C. Corros. Sci. **53**, 1983-1989 (2011). doi:10.1016/j.corsci.2011.02.020
[59] J. Xu, T. Shoji, C. Jang, The effects of dissolved hydrogen on the corrosion behavior of Alloy 182 in simulated primary water. Corros. Sci. **97**, 115-125 (2015). doi: 10.1016/j.corsci.2015.04.021
[60] R. Mendonça, R.-W. Bosch, W. Van Renterghem, et al., Effect of temperature and dissolved hydrogen on oxide films formed on Ni and Alloy 182 in simulated PWR water. J. Nucl. Mater. **477**, 280-291(2016). doi:10.1016/j.jnucmat.2016.05.022
[61] G.D. Han, Z.P. Lu, X.K. Ru, et al., Properties of oxide films formed on 316L SS and model alloys with modified Ni, Cr and Si contents in high temperature water. Corros. Sci. **106**, 157-171 (2016). doi:10.1016/j.corsci.2016.02.001
[62] G.D. Han, Z.P. Lu, X.K. Ru, et al., Improving the oxidation resistance of 316L stainless steel in simulated pressurized water reactor primary water by electropolishing treatment. J. Nucl. Mater. **467**, 194-204 (2015). doi:10.1016/j.jnucmat.2015.09.029
[63] Q.J. Peng, J. Hou, K. Sakaguchi, et al., Effect of dissolved hydrogen on corrosion of Inconel Alloy 600 in high temperature hydrogenated water. Electrochim. Acta **56**, 8375-8386 (2011). doi:10.1016/j.electacta.2011.07.032
[64] T.M. Cui, X.H. Xu, D. Pan, et al., Comparison of stress corrosion cracking susceptibilities of 308L and 309L cladding layers in high-temperature water with various dissolved oxygen concentrations. J. Nucl. Mater. **569**, 153913 (2022). doi:10.1016/j.jnucmat.2022.153913
[65] W.J. Kuang, X.Q. Wu, E.H. Han, Influence of dissolved oxygen concentration on the oxide film formed on 304 stainless steel in high temperature water. Corros. Sci. **63**, 259-266 (2012). doi:10.1016/j.corsci.2012.06.007
[66] C.S. Kumai, T.M. Devine, Influence of Oxygen Concentration of 288°C Water

and Alloy Composition on the Films Formed on Fe-Ni-Cr Alloys. Corros. **63**, 1101-1113 (2007). doi:10.5006/1.3278328
[67] M.F. Montemor, M.G.S. Ferreira, M. Walls, et al., Influence of pH on Properties of Oxide Films Formed on Type 316L Stainless Steel, Alloy 600, and Alloy 690 in High-Temperature Aqueous Environments. Corros. **59**, 11-21 (2003). doi:10.1016/S0927-0256(02)00403-2
[68] X.H. Liu, E.H. Han, X.Q. Wu, Effects of pH value on characteristics of oxide films on 316L stainless steel in Zn-injected borated and lithiated high temperature water. Corros. Sci. **78**, 200-207 (2014). doi:10.1016/j.corsci.2013.09.017
[69] R.P. Matthews, R.D. Knusten, J.E. Westraadt, et al., Intergranular oxidation of 316L stainless steel in the PWR primary water environment. Corros. Sci. **125**, 175-183 (2017). doi:10.1016/j.corsci.2017.06.023
[70] D.D. Macdonald, M. Urquidi-Macdonald, Theory of Steady‐State Passive Films. J. Electrochem. Soc. **137**, 2395 (1990). doi:10.1149/1.2152195
[71] X.D. Lin, Q.J. Peng, J.N. Mei, et al., Corrosion of phase and phase boundary in proton-irradiated 308L stainless steel weld metal in simulated PWR primary water. Corros. Sci. **165**, 108401 (2020). doi:10.1016/j.corsci.2019.108401
[72] T. Maekawa, M. Kagawa, N. Nakajima, Corrosion Behaviors of Stainless Steel in High-Temperature Water and Superheated Steam. Trans. Jpn. Inst. Met. **9**, 130-136 (1968). doi:10.2320/matertrans1960.9.130
[73] S. Lozano-Perez, K. Kruska, I. Iyengar, et al., The role of cold work and applied stress on surface oxidation of 304 stainless steel. Corros. Sci. **56**, 78-85 (2012). doi:10.1016/j.corsci.2011.11.021
[74] S. Lozano-Perez, T. Yamada, T. Terachi, et al., Multi-scale characterization of stress corrosion cracking of cold-worked stainless steels and the influence of Cr content. Acta. Mater. **57**, 5361-5381 (2009). doi:10.1016/j.actamat.2009.07.040
[75] G.S. Was, *Fundamentals of Radiation Materials Science: Metals and Alloys*. (Springer, Berlin, 2007).
[76] S. Perrin, L. Marchetti, C. Duhamel, et al., Influence of irradiation on the oxide film formed on 316L stainless steel in PWR primary water. Oxid. Met. **80**, 623-633 (2013). doi:10.1007/s11085-013-9401-3
[77] H. Liu, S.L. Min, M.L. Jiang, et al., Corrosion performance of $He^+$ ion irradiated 304L stainless steel made by laser powder bed fusion in simulated PWR water. Corros. Sci. **206**, 110545 (2022). doi:10.2139/ssrn.4049697
[78] S.K. Wang, Q. Wang, S.H. Zhang, et al., Clarifying the irradiation effect on the general oxidation of 316L stainless steel in high temperature hydrogenated water after

1000h immersion. Acta Mater. **255**, 119100 (2023). doi:10.1016/j.actamat.2023.119100
[79] Z.J. Zhang, E.H. Han, C. Xiang, Effect of helium ion irradiation on short-time corrosion behavior of two novel high-entropy alloys in simulated PWR primary water. Corros. Sci. **191**, 109742 (2021). doi:10.1016/j.corsci.2021.109742
[80] G.S. Was, J.T. Busby, T. Allen, et al., Emulation of neutron irradiation effects with protons: validation of principle. J. Nucl. Mater. **300**, 198-216 (2002). doi:10.1016/S0022-3115(01)00751-6
[81] S.H. Li, J.T. Li, W.Z. Han, Radiation-induced helium bubbles in metals. Materials **12**, 1036 (2019). doi:10.3390/ma12071036
[82] M. Dumerval, S. Perrin, L. Marchetti, et al., Effect of implantation defects on the corrosion of 316L stainless steels in primary medium of pressurized water reactors. Corros. Sci. **107**, 1-8 (2016). doi:10.1016/j.corsci.2016.02.007
[83] M. Sennour, L. Marchetti, S. Perrin, et al., Characterization of the oxide films formed at the surface of Ni-base alloys in pressurized water reactors primary coolant by transmission electron microscopy. Mater. Sci. Forum **595-598**, 539-547 (2008). doi:10.4028/www.scientific.net/MSF.595-598.539
[84] K. Fukuya, H. Nishioka, K. Fujii, et al., Characterization of surface oxides formed on irradiated stainless steels in simulated PWR primary water. Paper presented at Proceedings of Fontevraud 8: Conference on Contribution of Materials Investigations and Operating Experience to LWRs' Safety, Performance and Reliability, Avignon (France), 15–18 September 2014
[85] W.S. Wu, G. Ran, Y.P. Li, et al., Early corrosion behaviour of irradiated FeCrAl alloy in a simulated pressurized water reactor environment. Corros. Sci. **174**, 108824 (2020). doi:10.1016/j.corsci.2020.108824
[86] S.S. Raiman, G.S. Was, Accelerated corrosion and oxide dissolution in 316L stainless steel irradiated in situ in high temperature water. J. Nucl. Mater. **493**, 207-218 (2017). doi:10.1016/j.jnucmat.2017.05.043
[87] T. Fukumura, K. Fukuya, K. Fujii, et al., in Proceedings of the 18th International Conference on Environmental Degradation of Materials in Nuclear Power Systems – Water Reactors, ed. by J.H. Jackson, D. Paraventi, M. Wright. The Minerals, Metals & Materials Series. (Springer, Cham, 2019), pp. 2153-2163
[88] P. Wang, G.S. Was, Oxidation of Zircaloy-4 during in situ proton irradiation and corrosion in PWR primary water. J. Mater. Res. **30**, 1335-1348 (2015). doi: 10.1557/jmr.2014.408
[89] X.D. Lin, E.H. Han, Q.J. Peng, et al., Effect of post-irradiation annealing on microstructure and corrosion of proton-irradiated 308L stainless steel weld metal.

Corros. Sci. **175**, 108887 (2020). doi:10.1016/j.corsci.2020.108887
[90] H. Lefaix-Jeuland, L. Marchetti, S. Perrin, et al., Oxidation kinetics and mechanisms of Ni-base alloys in pressurised water reactor primary conditions: Influence of subsurface defects. Corros. Sci. **53**, 3914-3922 (2011). doi:10.1016/j.corsci.2011.07.024
[91] M. Warzee, J. Hennaut, M. Maurice, et al., Effect of Surface Treatment on the Corrosion of Stainless Steels in High-Temperature Water and Steam. J. Electrochem. Soc. **112**, 670 (1965). doi:10.1149/1.2423661
[92] S.E. Ziemniak, M. Hanson, P.C. Sander, Electropolishing effects on corrosion behavior of 304 stainless steel in high temperature, hydrogenated water. Corros. Sci. **50**, 2465-2477 (2008). doi:10.1016/j.corsci.2008.06.032
[93] C. Pokor, Y. Brechet, P. Dubuisson, et al., Irradiation damage in 304 and 316 stainless steels: Experimental investigation and modeling. Part I: Evolution of the microstructure. J. Nucl. Mater. **326**, 19-29 (2004). doi:10.1016/j.jnucmat.2003.11.007
[94] S.K. Wang, S.H. Zhang, J.Y. Xie, et al., Clarifying the mitigation effect of proton irradiation on the intergranular oxidation of 316L stainless steel in high temperature water. Acta Mater. **241**, 118408 (2022). doi:10.1016/j.actamat.2022.118408
[95] W.J. Kuang, J. Hesterberg, G.S. Was, The effect of post-irradiation annealing on the stress corrosion crack growth rate of neutron-irradiated 304L stainless steel in boiling water reactor environment. Corros. Sci. **161**, 108183 (2019). doi:10.1016/j.corsci.2019.108183
[96] P. Deng, Q.J. Peng, E.H. Han, Grain boundary oxidation of proton-irradiated nuclear grade stainless steel in simulated primary water of pressurized water reactor. Sci. Rep. **11**, 1371 (2021). doi:10.1038/s41598-020-80600-x
[97] P. Deng, Q.J. Peng, E.H. Han, et al., Proton irradiation assisted localized corrosion and stress corrosion cracking in 304 nuclear grade stainless steel in simulated primary PWR water, J. Mater. Sci. Technol. **65**, 61-71 (2021). doi:10.1016/j.jmst.2020.04.068
[98] S. Swaminathan, K. Sun, G.S. Was, Decoupling the roles of grain boundary oxidation and stress in IASCC of neutron-irradiated 304L stainless steel. J. Nucl. Mater. **585**, 154604 (2023). doi:10.1016/j.jnucmat.2023.154604
[99] L.J. Dong, Q.J. Peng, E.H. Han, et al., Stress corrosion cracking in the heat affected zone of a stainless steel 308L-316L weld joint in primary water. Corros. Sci. **107**, 172-181 (2016). doi:10.1016/j.corsci.2016.02.030
[100] T. Terachi, T. Yamada, N. Totsuka, et al., in Proceedings of the 18th International Conference on Environmental Degradation of Materials in Nuclear Power Systems – Water Reactors, ed. by J.H. Jackson, D. Paraventi, M. Wright. The

Minerals, Metals & Materials Series. (Springer, Cham, 2019), pp. 105-108
[101] K. Fukuya, Current understanding of radiation-induced degradation in light water reactor structural materials. J. Nucl. Sci. Technol. **50**, 213-254 (2013). doi:10.1080/00223131.2013.772448
[102] K. Fukuya, K. Fujii, H. Nishioka, et al., Evolution of Microstructure and Microchemistry in Cold-worked 316 Stainless Steels under PWR Irradiation. J. Nucl. Sci. Technol. **43**, 159-173 (2006). doi:10.1080/18811248.2006.9711078
[103] D.J. Edwards, E.P. Simonen, F.A. Garner, et al., Influence of irradiation temperature and dose gradients on the microstructural evolution in neutron-irradiated 316SS. J. Nucl. Mater. **317**, 32-45 (2003). doi:10.1016/S0022-3115(03)00003-5
[104] C.M. Barr, G.A. Vetterick, K.A. Unocic, et al., Anisotropic radiation-induced segregation in 316L austenitic stainless steel with grain boundary character. Acta Mater. **67**, 145-155 (2014). doi:10.1016/j.actamat.2013.11.060
[105] S. Watanabe, Y. Takamatsu, N. Sakaguchi, et al., Sink effect of grain boundary on radiation-induced segregation in austenitic stainless steel. J. Nucl. Mater. **283-287**, 152-156 (2000). doi:10.1016/S0022-3115(00)00204-X
[106] Y.S. Lim, S.W. Kim, S.S. Hwang, et al., Intergranular oxidation of Ni-based Alloy 600 in a simulated PWR primary water environment. Corros. Sci. **108**, 125-133 (2016). doi:10.1016/j.corsci.2016.02.040
[107] B. Pastina, J. Isabey, B. Hickel, The influence of water chemistry on the radiolysis of the primary coolant water in pressurized water reactors. J. Nucl. Mater. **264**, 309-318 (1999). doi:10.1016/S0022-3115(98)00494-2
[108] G.S. Was, P.L. Andresen, Stress Corrosion Cracking Behavior of Alloys in Aggressive Nuclear Reactor Core Environments. Corros. **63**, 19-45 (2007). doi:10.5006/1.3278331
[109] K. Ishigure, Radiation chemistry related to nuclear power technology. Radiation Physics and Chemistry **22**, 119-129 (1983). doi:10.1016/0146-5724(83)90198-X
[110] M. Wang, S. Perrin, C. Corbel, et al., Electrochemical behaviour of 316L stainless steel exposed to representative chemistry in pressurised water reactors under proton radiation. J. Electroanal. Chem. **737**, 141-149 (2015). doi:10.1016/j.jelechem.2014.10.015
[111] Y.J. Kim, P.L. Andresen, Data Quality, Issues, and Guidelines for Electrochemical Corrosion Potential Measurement in High-Temperature Water. Corros. **59**, 584-596 (2003). doi:10.5006/1.3277589
[112] M. Tachibana, K. Ishida，Y. Wada，et al., Cathodic polarization properties of hydrogen peroxide and the effect on electrochemical corrosion potential calculation under simulated BWR environment. Paper presented at NACE - International

Corrosion Conference Series, Orlando, FL (USA), 17-21 Mar 2013
[113] G. Bellanger, Effect of pH and hydrogen peroxide in radioactive water on the passivity of 1018 carbon steel. J. Mater. Sci. **30**, 1259-1265 (1995). doi:10.1007/BF00356128
[114] T. Miyazawa, T. Terachi, S. Uchida, et al., Effects of hydrogen peroxide on corrosion of stainless steel, (V) characterization of oxide film with multilateral surface analyses. J. Nucl. Sci. Technol. **43**, 884-895 (2006). doi:10.1080/18811248.2006.9711173
[115] S.S. Raiman, D.M. Bartels, G.S. Was, Radiolysis driven changes to oxide stability during irradiation-corrosion of 316L stainless steel in high temperature water. J. Nucl. Mater. **493**, 40-52 (2017). doi:10.1016/j.jnucmat.2017.05.042
[116] R.D. Hanbury, G.S. Was, Oxide growth and dissolution on 316L stainless steel during irradiation in high temperature water. Corros. Sci. **157**, 305-311 (2019). doi:10.1016/j.corsci.2019.06.006
[117] P. Wang, S. Grdanovska, D.M. Bartels, et al., Effect of radiation damage and water radiolysis on corrosion of FeCrAl alloys in hydrogenated water. J. Nucl. Mater. **533**, 152108 (2020). doi:10.1016/j.jnucmat.2020.152108
[118] G.S. Was, P. Wang, in Proceedings of the 18th International Conference on Environmental Degradation of Materials in Nuclear Power Systems – Water Reactors, ed. by J.H. Jackson, D. Paraventi, M. Wright, Oregon (USA), 07 October 2017. The Minerals, Metals & Materials Series (Springer, Cham, 2019), pp. 1461-1474
[119] R.D. Hanbury, G.S. Was, in Proceedings of the 18th International Conference on Environmental Degradation of Materials in Nuclear Power Systems – Water Reactors, ed. by J.H. Jackson, D. Paraventi, M. Wright, Oregon (USA), 07 October 2017. The Minerals, Metals & Materials Series (Springer, Cham, 2019), p. 2303-2312
[120] D.F. Williams, Assessment of candidate molten salt coolants for the advanced high temperature reactor (AHTR) (Oak Ridge National Laboratory, Oak Ridge, 2006).
[121] L.S. Richardson, D.C. Vreeland, W.D. Manly, Corrosion by molten fluorides (Oak Ridge National Laboratory, Oak Ridge, 1952)
[122] J.H. Devan, R.B. Evans, Corrosion behavior of reactor materials in fluoride salt mixtures (Oak Ridge National Laboratory, Oak Ridge, 1962)
[123] R.J. Kedl, The migration of a class of fission products (noble metals) in the molten-salt reactor experiment (Oak Ridge National Laboratory, Oak Ridge, 1972).
[124] L.C. Olson, J.W. Ambrosek, K. Sridharan, et al. Materials corrosion in molten LiF-NaF-KF salt. J. Fluor. Chem. **130**, 67-73 (2009). doi:10.1016/j.jfluchem.2008.05.008
[125] J. Koger, Mass transfer between Hastelloy N and a molten sodium fluoroborate

mixture in a thermal convection loop (Oak Ridge National Laboratory, Oak Ridge, 1972)
[126] F.Y. Ouyang, C.H. Chang, B.C. You, et al., Effect of moisture on corrosion of Ni-based alloys in molten alkali fluoride FLiNaK salt environments. J. Nucl. Mater. **437**, 201-207 (2013). doi:10.1016/j.jnucmat.2013.02.021
[127] F.Y. Ouyang, C.H. Chang, J.J. Kai, Long-term corrosion behaviors of Hastelloy-N and Hastelloy-B3 in moisture-containing molten FLiNaK salt environments. J. Nucl. Mater. **446**, 81-89 (2014). doi:10.1016/j.jnucmat.2013.11.045
[128] X.X. Ye, H. Ai, Z. Guo, et al., The high-temperature corrosion of Hastelloy N alloy (UNS N10003) in molten fluoride salts analyzed by STXM, XAS, XRD, SEM, EPMA, TEM/EDS. Corros. Sci. **106**, 249-259 (2016). doi:10.1016/j.corsci.2016.02.010
[129] H.Q. Yin, J. Qiu, H.J. Liu, Effect of $CrF_3$ on the corrosion behaviour of Hastelloy-N and 316L stainless steel alloys in FLiNaK molten salt. Corros. Sci. **131**, 355-364 (2018). doi:10.1016/j.corsci.2017.12.008
[130] C. Nourry, P. Souček, L. Massot, et al., Electrochemistry of uranium in molten LiF-$CaF_2$. J. Nucl. Mater. **430**, 58-63 (2012). doi:10.1016/j.jnucmat.2012.06.028
[131] M. Gibilaro, L. Massot, P. Chamelot, et al., Study of neodymium extraction in molten fluorides by electrochemical co-reduction with aluminium. J. Nucl. Mater. **382**, 39-45 (2008). doi:10.1016/j.jnucmat.2008.09.004
[132] P. Taxil, L. Massot, C. Nourry, et al., Lanthanides extraction processes in molten fluoride media: Application to nuclear spent fuel reprocessing. J. Fluorine Chem. **130**, 94-101 (2009). doi:10.1016/j.jfluchem.2008.07.004
[133] H.E. McCoy, Intergranular cracking of structural materials exposed to fuel salt (Oak Ridge National Laboratory, Oak Ridge, 1972)
[134] P.T. Carlson, L.C. Manley, H.E. McCoy, et al., The isothermal diffusion of 127Te tracer in Hastelloy N, Ni-200, and type 304L stainless steel specimens (Oak Ridge National Laboratory, Oak Ridge, 1973)
[135] M.W. Rosenthal, P.N. Haubenreich, R.B. Briggs, The development status of molten-salt reactors (Oak Ridge National Laboratory, Oak Ridge, 1972)
[136] J. Koger, Corrosion and Mass Transfer Characteristics of $NaBF_4$-NaF (92-8 mole%) in Hastelloy N (Oak Ridge National Laboratory, Oak Ridge, 1972)
[137] J.H. Devan, Dissertation, Oak Ridge National Laboratory, 1969
[138] C. Ellis, W. Thompson, The Aircraft Nuclear Propulsion Project Quarterly Progress Report For Period Ending AUGUST 31 (Oak Ridge National Laboratory, Oak Ridge, 1950)
[139] W. Cottrell, Aircraft Nuclear Propulsion Project Quarterly Progress Report For

Period Ending MARCH 10 (Oak Ridge National Laboratory, Oak Ridge, 1952).
[140] W. Jordan, S. Cromer, R. Strough, et al., Aircraft Nuclear Propulsion Project Quarterly Progress Report For Period Ending December 10 (Oak Ridge National Laboratory, Oak Ridge, 1954)
[141] H. Inouye, W.D. Manly, K. Roche, U.S. Patent 2921850, 19 Jan. 1960.
[142] H.E. McCoy, The INOR-8 Story (Oak Ridge National Laboratory, Oak Ridge, 1969)
[143] G.Q. Zheng, Dissertation, University of Wisconsin-Madison, 2015
[144] K.A. Misra, J.D. Whittenberger, Fluoride Salts and Container Materials for Thermal Energy Storage Applications in the Temperature Range 973 to 1400 K (National Aeronautics and Space Administration, Cleveland, OH (USA), 1987)
[145] J.X. Dai, C.F. He, C.L. Ren, et al., Concentration and solvent effects on structural and thermodynamic properties of uranium (Ⅳ) fluoride by molecular dynamic simulation. J. Nucl. Mater. **576**, 154266 (2023). doi:10.1016/j.jnucmat.2023.154266
[146] C.L. Ren, H. Han, W.B. Gong, et al., Adsorption and diffusion of fluorine on Cr-doped Ni (111) surface: Fluorine-induced initial corrosion of non-passivated Ni-based alloy. J. Nucl. Mater. **478**, 295-302 (2016). doi:10.1016/j.jnucmat.2016.06.027
[147] J.X. Dai, W. Zhang, C.L. Ren, et al., Prediction of dynamics properties of $ThF_4$-based fluoride molten salts by molecular dynamic simulation. J. Mol. Liq. **318**, 114059 (2020). doi:10.1016/j.molliq.2020.114059
[148] D.F. Williams, D.F. Wilson, J.R. Keiser, et al., Research on Molten Fluorides as High Temperature Heat Transfer Agents (Oak Ridge National Laboratory, Oak Ridge, 2003).
[149] R.E. Thoma, Chemical Aspects of MSRE Operations (Oak Ridge National Laboratory, Oak Ridge, 1971)
[150] J.W. Koger, Evaluation of hastelloy N alloys after nine years exposure to both a molten fluoride salt and air at temperatures from 700 to 560℃ (Oak Ridge National Laboratory, Oak Ridge, 1972)
[151] J.W. Koger, A forced- Circulation loop for corrosion studies: Hastelloy N compatibility with $NaBF_4$-NaF (92-8 mole%) (Oak Ridge National Laboratory, Oak Ridge, 1972).
[152] R.B. Briggs, Molten salt reactor program progress report (Oak Ridge National Laboratory, Oak Ridge, 1962).
[153] L.C. Olson, J. W. Ambrosek, K. Sridharan, et al., Materials corrosion in molten

LiF-NaF-KF salt. J. Fluor. Chem. **130**, 67-73 (2009). doi:10.1016/j.jfluchem.2008.05.008
[154] W.D. Xue, X.M. Yang, X.X. Ye, et al., Effects of silicon carbide on the corrosion of metallic materials in molten LiF-NaF-KF salt. Corros. Sci. **143**, 157-165 (2018). doi:10.1016/j.corsci.2018.08.023
[155] H. Ai, J. Hou, X.X. Ye, et al., Influence of graphite-alloy interactions on corrosion of Ni-Mo-Cr alloy in molten fluorides. J. Nucl. Mater. **503**, 116-123 (2018). doi:10.1016/j.jnucmat.2018.03.001
[156] Y.L. Wang, H.J. Liu, C.L. Zeng, Galvanic corrosion of pure metals in molten fluorides. J. Fluor. Chem. **165**, 1-6 (2014). doi:10.1016/j.jfluchem.2014.05.010
[157] K.L. Murty, I. Charit, *An introduction to nuclear materials: Fundamentals and Applications* (Wiley-VCH, Berlin, 2013)
[158] J. Knaster, A. Moeslang, T. Muroga, Materials research for fusion. Nat. Phys. **12**, 424-434 (2016). doi:10.1038/nphys3735
[159] H. Trinkaus, B.N. Singh, Helium accumulation in metals during irradiation – where do we stand? J. Nucl. Mater. **323**, 229-242 (2003). doi:10.1016/j.jnucmat.2003.09.001
[160] H.E. McCoy, An Evaluation of the Molten Salt Reactor Experiment Hastelloy N Survellance Specimens, First Group (Oak Ridge National Laboratory, Oak Ridge, 1967)
[161] H.E. McCoy, An Evaluation of the Molten Salt Reactor Experiment Hastelloy N Survellance Specimens, Second Group (Oak Ridge National Laboratory, Oak Ridge, 1969)
[162] H.E. McCoy, An Evaluation of the Molten Salt Reactor Experiment Hastelloy N Survellance Specimens, Third Group (Oak Ridge National Laboratory, Oak Ridge, 1970)
[163] H.E. McCoy, An Evaluation of the Molten Salt Reactor Experiment Hastelloy N Survellance Specimens, Fourth Group (Oak Ridge National Laboratory, Oak Ridge, 1971)
[164] G.S. Was, M. Hash, G. Odette, Hardening and microstructure evolution in proton-irradiated model and commercial pressure-vessel steels. Microstructural Processes in Irradiated Materials. Paper presented at the Symposium Held as Part of the 2003 TMS Annual Meeting, San Diego, California, 2-6 March 2003
[165] H.E. McCoy, R.L. Beatty, W.H. Cook, et al., New Developments in Materials for Molten-Salt Reactors. Nucl. Appl. Technol. **8**, 156-169 (1970). doi:10.13182/NT70-A28622
[166] J.R. DiStefano, J.H. DeVan, J.R. Keiser, et al., Materials consideration for

molten salt accelerator-based plutonium conversion systems (Oak Ridge National Laboratory, Oak Ridge, 1995)
[167] H.E. McCoy, B. McNobb, Intergranular cracking of INOR 8 in the MSRE (Oak Ridge National Laboratory, Oak Ridge, 1972)
[168] H.L. Zhu, R. Holmes, T. Hanley, et al., High-temperature corrosion of helium ion-irradiated Ni-based alloy in fluoride molten salt. Corros. Sci. **91**, 1-6 (2015). doi:10.1016/j.corsci.2014.11.013
[169] H.L. Zhu, R. Holmes, T. Hanley, et al., Effects of bubbles on high-temperature corrosion of helium ion-irradiated Ni-based alloy in fluoride molten salt. Corros. Sci. **125**, 184-193 (2017). doi:10.1016/j.corsci.2017.06.027
[170] M. Liu, J. Hou, F.F. Han, et al., Effects of He ion irradiation on the corrosion performance of alloy GH3535 welded joint in molten FLiNaK. Corros. Sci. **146**, 172-178 (2019). doi:10.1016/j.corsci.2018.10.038
[171] G.H. Lei, S.D. Yang, H.F. Huang, et al., Corrosion-driven outward migration and growth of helium bubbles in a nickel-based alloy under high temperature molten salt environment. Corros. Sci. **153**, 47-52 (2019). doi:10.1016/j.corsci.2019.03.026
[172] G.H. Lei, C. Li, Z. Jiang, et al., Irradiation accelerated fluoride molten salt corrosion of nickel-based UNS N10003 alloy revealed by X-ray absorption fine structure. Corros. Sci. **165**, 108408 (2020). doi:10.1016/j.corsci.2019.108408
[173] Z.B. Zhu, H.F. Huang, G.H. Lei, et al., Synergistic effect of irradiation and molten salt corrosion: Acceleration or deceleration. Corros. Sci. **185**, 109434 (2021). doi:10.1016/j.corsci.2021.109434
[174] J.B. Lin, A.G. Li, S.M. He, et al., Investigation on corrosion resistance of Hastelloy N alloy after $He^+$ ion irradiation. Nucl. Tech. **37**, 050601 (2014). doi: 10.11889/j.0253-3219.2014.hjs.37.050601
[175] G.H. Lei, S.D. Yang, R.D. Liu, et al., The effect of He bubbles on the corrosion properties of nickel-based alloy in molten salt environment. Nucl. Tech. **42**, 060402 (2019). doi:10.11889/j.0253-3219.2019.hjs.42.040602.
[176] W.Y. Zhou, Y. Yang, G.Q. Zheng, et al., Proton irradiation-decelerated intergranular corrosion of Ni-Cr alloys in molten salt. Nat. Commun. **11**, 3430 (2020). doi:10.1038/s41467-020-17244-y
[177] N.D.B. Ezell, S. Raiman, J.M. Kurley, et al., Neutron Irradiation of Alloy N and 316L Stainless Steel in Contact with a Molten Chloride Salt. Nucl. Eng. Technol. **53**, 920-926 (2021). doi:10.31224/osf.io/e3yru
[178] S.M. Bruemmer, E.P. Simonen, P.M. Scott, et al., Radiation induced material changes and susceptibility to intergranular failure of light-water-reactor core internals. J. Nucl. Mater. **274**, 299-314 (1999). doi:10.1016/S0022-3115(99)00075-6

[179] S.J. Zinkle, J.T. Busby, Structural materials for fission & fusion energy. Mater. Today **12**, 12-19 (2009). doi:10.1016/S1369-7021(09)70294-9
[180] Y. Nemoto, A. Hasegawa, M. Satou, et al., Microstructural development and radiation hardening of neutron irradiated Mo–Re alloys. J. Nucl. Mater. **324**, 62-70 (2004). doi:10.1016/S0140-6701(04)80579-4
[181] M. Liu, Dissertation, The University of Chinese Academy of Sciences, Shanghai, 2015.
[182] H.F. Huang, J. Gao, B. Radiguet, et al., Microstructural evolution and hardening of GH3535 alloy under energetic Xe ion irradiation at room temperature and 650 °C. J. Nucl. Mater. **499**, 431-439 (2018). doi:10.1016/j.jnucmat.2017.12.006
[183] Y.Y. Jia, H.W. Cheng, J. Qiu, et al., Effect of temperature on diffusion behavior of Te into nickel. J. Nucl. Mater. **441**, 372-379 (2013). doi:10.1016/j.jnucmat.2013.06.025
[184] H.W. Cheng, F.F. Han, Y.Y. Jia, et al., Effects of Te on intergranular embrittlement of a Ni-16Mo-7Cr alloy. J. Nucl. Mater. **461**, 122-128 (2015). doi:10.1016/j.jnucmat.2015.01.049
[185] F.F. Han, X.D. Wang, Y.Y. Jia, et al., Effect of grain boundary carbides on the diffusion behavior of Te in Ni-16Mo-7Cr base superalloy. Mater. Charact. **164**, 110329 (2020). doi:10.1016/j.matchar.2020.110329
[186] L. Jiang, W. Wang, X.X. Ye, et al., Unexpected effect of hydroxyl radical on tellurium corrosion of the Ni-Mo-Cr–Nb based alloy. Corros. Sci. **173**, 108748 (2020). doi:10.1016/j.corsci.2020.108748
[187] J.H. DeVan, J.R. DiStefano, W.P. Eatherly, et al., Materials considerations for molten salt accelerator‐based plutonium conversion systems (Oak Ridge National Laboratory, Oak Ridge, 1995).
[188] H.E. McCoy, Status of materials development for molten salt reactors (Oak Ridge National Laboratory, Oak Ridge, 1987)
[189] L.E. McNeese, Semiannual progress report for period ending (Oak Ridge National Laboratory, Oak Ridge, 1976)
[190] B. Huang, C. Zhang, G. Zhang, et al., Wear and corrosion resistant performance of thermal-sprayed Fe-based amorphous coatings: A review. Surf. Coat. Technol. **377**, 124896 (2019). doi:10.1016/j.surfcoat.2019.124896
[191] A.S.H. Makhlouf, Current and advanced coating technologies for industrial applications. Nanocoatings and Ultra-Thin Films: Technologies and applications, 3-23 (2011). doi:10.1533/9780857094902.1.3
[192] J.R. Conrad, J.L. Radtke, R.A. Dodd, et al., Plasma source ion-implantation

technique for surface modification of materials. J. Appl. Phys. **62**, 4591-4596 (1987). doi:10.1063/1.339055
[193] S. Isogawa, H. Tojo, A. Chayahara, et al., Plasma based ion implantation technology for high-temperature oxidation-resistant surface coatings. Surf. Coat. Technol. **158-159**, 186-192 (2002). doi:10.1016/S0257-8972(02)00202-5
[194] K. Sridharan, S.P. Harrington, A.K. Johnson, et al., Oxidation of plasma surface modified zirconium alloy in pressurized high temperature water. Mater. Des. **28**, 1177-1185 (2007). doi:10.1016/j.matdes.2006.01.019
[195] F. Nasirpouri, K. Alipour, F. Daneshvar, et al., Electrodeposition of anticorrosion nanocoatings. Corrosion Protection at the Nanoscale: Micro and Nano Technologies, 473-497 (2020). doi:10.1016/B978-0-12-819359-4.00024-6
[196] Z.X. Zeng, A. Liang, J.Y. Zhang, Electrochemical corrosion behavior of chromium–phosphorus coatings electrodeposited from trivalent chromium baths. Electrochim. Acta. **53**, 7344-7349 (2008). doi:10.1016/j.electacta.2008.03.081
[197] Y.F. Gu, Y.W. Xu, Y. Shi, et al., Corrosion resistance of 316 stainless steel in a simulated pressurized water reactor improved by laser cladding with chromium. Surf. Coat. Technol. **441**, 128534 (2022). doi:10.1016/j.surfcoat.2022.128534
[198] L. Olson, K. Sridharan, M. Anderson, et al., Nickel-plating for active metal dissolution resistance in molten fluoride salts. J. Nucl. Mater. **411**, 51-59 (2011). doi:10.1016/j.jnucmat.2011.01.032
[199] W.L. Chen, X.Y. Ding, Y.C. Feng, et al., Vacancy formation enthalpies of high-entropy FeCoCrNi alloy via first-principles calculations and possible implications to its superior radiation tolerance. J. Mater. Sci. Technol. **34**, 355-364 (2018). doi:10.1016/j.jmst.2017.11.005
[200] Z.P. Wang, Q.H. Fang, J. Li, et al., Effect of lattice distortion on solid solution strengthening of BCC high-entropy alloys. J. Mater. Sci. Technol. **34**, 349-354 (2018). doi:10.1016/j.jmst.2017.07.013
[201] S.Q. Xia, M.C. Gao, T.F. Yang, et al., Phase stability and microstructures of high entropy alloys ion irradiated to high doses. J. Nucl. Mater. **480**, 100-108 (2016). doi:10.1016/j.jnucmat.2016.08.017
[202] Y.W. Zhang, G.M. Stocks, K. Jin, et al., Influence of chemical disorder on energy dissipation and defect evolution in concentrated solid solution alloys. Nat. Commun. 6, 8736 (2015). doi:10.1038/ncomms9736
[203] S.J. Zheng, S. Shao, J. Zhang, et al., Adhesion of voids to bimetal interfaces with non-uniform energies. Sci. Rep. **5**, 15428 (2015). doi:10.1038/SREP15428
[204] S.J. Zheng, I.J. Beyerlein, J.S. Carpenter, et al., High-strength and thermally stable bulk nanolayered composites due to twin-induced interfaces. Nat. Commun. **4**,

1696 (2013). doi:10.1038/ncomms2651
[205] G.R. Odette, M.J. Alinger, B.D. Wirth. Recent developments in irradiation-resistant steels. Annu. Rev. Mater. Res. **38**, 471-503 (2008). doi:10.1146/annurev.matsci.38.060407.130315
[206] A. Hirata, T. Fujita, Y.R. Wen, et al., Atomic structure of nanoclusters in oxide-dispersion-strengthened steels. Nat. Mater. **10**, 922-926 (2011). doi:10.1038/nmat3150
[207] H.F. Huang, C. Yang, M.D.L. Reyes, Effect of Milling Time on the Microstructure and Tensile Properties of Ultrafine Grained Ni–SiC Composites at Room Temperature. J. Mater. Sci. Technol. **31**, 923-929 (2015). doi:10.1016/j.jmst.2014.12.009
[208] H.F. Huang, W. Zhang, M.D.L. Reyes, et al., Mitigation of He embrittlement and swelling in nickel by dispersed SiC nanoparticles. Mater. Design **90**, 359-363 (2016). doi:10.1016/j.matdes.2015.10.147
[209] C. Yang, H.F. Huang, X.L. Zhou, High-temperature stability of Ni-3 wt.% SiCNP composite and the effect of milling time. J. Nucl. Mater. **467**, 635-643 (2015). doi:10.1016/j.jnucmat.2015.10.044
[210] X.L. Zhou, H.F. Huang, R. Xie, et al., Helium ion irradiation behavior of Ni-1wt.%SiCNP composite and the effect of ion flux. J. Nucl. Mater. **467**, 848-854 (2015). doi:10.1016/j.jnucmat.2015.11.004
[211] K. Saeidi, L. Kvetková, F. Lofaj, et al., Austenitic stainless steel strengthened by the in situ formation of oxide nanoinclusions. RSC Adv. **5**, 20747-20750 (2015). doi:10.1039/c4ra16721j
[212] M.S. Pham, B. Dovgyy, P.A. Hooper, Twinning induced plasticity in austenitic stainless steel 316L made by additive manufacturing. Mater. Sci. Eng. A **704**, 102-111 (2017). doi:10.1016/j.msea.2017.07.082
[213] J. Ren, L.M. Yu, Y.C. Liu, et al., Corrosion behavior of an Al added high-Cr ODS steel in supercritical water at 600 °C. Appl. Surf. Sci. **480**, 969-978 (2019). doi:10.1016/j.corsci.2021.110008
[214] C. Li, G.H. Lei, J.Z. Liu, et al., A potential candidate structural material for molten salt reactor: ODS nickel-based alloy. J. Mater. Sci. Technol. **109**, 129-139 (2022). doi:10.1016/j.jmst.2021.08.071
[215] R.S. Pathania, B. Cheng, M. Dove, et al. In Fontevraud 4: Contribution of materials investigation to the resolution of problems encountered in pressurized water reactors, Paris (France), 14-18 September 1998
[216] S.E. Ziemniak, M. Hanson, Zinc treatment effects on corrosion behavior of Alloy 600 in high temperature, hydrogenated water. Corros. Sci. **48**, 3330-3348

(2006). doi:10.1016/j.corsci.2005.11.002
[217] S.E. Ziemniak, M. Hanson, Zinc treatment effects on corrosion behavior of 304 stainless steel in high temperature, hydrogenated water. Corros. Sci. **48**, 2525-2546 (2006). doi:10.1016/j.corsci.2005.11.002
[218] I. Betova, M. Bojinov, P. Kinnunen, et al., Influence of Zn on the oxide layer on AISI 316L(NG) stainless steel in simulated pressurised water reactor coolant. Electrochim. Acta. **54**, 1056-1069 (2009). doi:10.1016/j.electacta.2008.08.040
[219] L.F. Zhang, K. Chen, J.M. Wang, et al., Effects of zinc injection on stress corrosion cracking of cold worked austenitic stainless steel in high-temperature water environments. Scripta. Mater. **140**, 50-54 (2017). doi:10.1016/j.scriptamat.2017.05.032
[220] K. Norring, J. Engström, Initiation of SCC in nickel base alloys in primary PWR environment: studies at Studsvik since mid 1980s. Energy Materials: Materials Science and Engineering for Energy Systems **3**, 113-118 (2008). doi:10.1179/174892408X394227
[221] S.H. Jeon, E.H. Lee, D.H. Hur, Effects of dissolved hydrogen on general corrosion behavior and oxide films of alloy 690TT in PWR primary water. J. Nucl. Mater. **485**, 113-121 (2017). doi:10.1016/j.jnucmat.2016.12.020
[222] T. Kim, K.J. Choi, S.C. Yoo, et al., Effects of dissolved hydrogen on the crack-initiation and oxidation behavior of nickel-based alloys in high-temperature water. Corros. Sci. **106**, 260-270 (2016). doi:10.1016/j.corsci.2016.02.011
[223] T. Terachi, N. Totsuka, T. Yamada, et al., Influence of dissolved hydrogen on structure of oxide film on alloy 600 formed in primary water of pressurized water reactors. J. Nucl. Sci. Technol. **40**, 509-516 (2003). doi:10.1080/18811248.2003.9715385
[224] L.J. Dong, Q.J. Peng, Z.M. Zhang, et al., Effect of dissolved hydrogen on corrosion of 316NG stainless steel in high temperature water. Nucl. Eng. Des. **295**, 403-414 (2015). doi:10.1016/j.nucengdes.2015.08.030
[225] D.R. Olander, P. Van Uffelen, On the role of grain boundary diffusion in fission gas release. J. Nucl. Mater. **288**, 137-147 (2001). doi:10.1016/S0022-3115(00)00725-X
[226] J.R. Keiser, J.H. DeVan, E.J. Lawrence, Compatibility of molten salts with type 316 stainless steel and lithium. J. Nucl. Mater. **85-86**, 295-298 (1979). doi:10.1016/0022-3115(79)90505-1
[227] C. Bessada, D. Zanghi, M. Salanne, et al., Investigation of ionic local structure in molten salt fast reactor LiF-ThF4-UF4 fuel by EXAFS experiments and molecular dynamics simulations. J. Mol. Liq. **307**, 112927 (2020).

doi:10.1016/j.molliq.2020.112927
[228] S.Q. Guo, J.S. Zhang, W. Wu, et al., Corrosion in the molten fluoride and chloride salts and materials development for nuclear applications. Prog. Mater. Sci. **97**, 448-487 (2018). doi:10.1016/j.pmatsci.2018.05.003
[229] Z.Y. Zhu, F.F. Han, Y.Y. Jia et al., Effect of yttrium on intergranular embrittlement behavior of GH3535 alloy induced by tellurium. Corros. Sci. **216**, 111091 (2023). doi:10.1016/j.corsci.2023.111091
[230] F.F. Han, Y.Y. Jia, Z.Y. Zhu, et al., Influence of lanthanum element on tellurium induced embrittlement of Ni-16Mo-7Cr alloy. Corros. Sci. **203**, 110360 (2022). doi:10.1016/j.corsci.2022.110360
[231] P. Yvon, F. Carré, Structural materials challenges for advanced reactor systems. J. Nucl. Mater. **385**, 217-222 (2009). doi:10.1016/j.jnucmat.2008.11.026